Accepted by Phys. Plasmas (Oct 15, 2014)

The effect of shock dynamics on compressibility of ignition-scale NIF implosions

A. B. Zylstra,[1, a)] J. A. Frenje,[1] F. H. Séguin,[1] D. G. Hicks,[2] E. Dewald,[2] H. Robey,[2] J. R. Rygg,[2] N. B. Meezan,[2] M. J. Rosenberg,[1] H. G. Rinderknecht,[1] S. Friedrich,[2] R. Bionta,[2] R. Olson,[3, 4] J. Atherton,[2] M. Barrios,[2] P. Bell,[2] R. Benedetti,[2] L. Berzak Hopkins,[2] R. Betti,[5] D. Bradley,[2] D. Callahan,[2] D. Casey,[2] G. Collins,[2] S. Dixit,[2] T. Döppner,[2] D. Edgell,[5] M. J. Edwards,[2] M. Gatu Johnson,[1] S. Glenn,[2] S. Glenzer,[2] G. Grim,[4] S. Hatchett,[2] O. Jones,[2] S. Khan,[2] J. Kilkenny,[6] J. Kline,[4] J. Knauer,[5] A. Kritcher,[2] G. Kyrala,[4] O. Landen,[2] S. LePape,[2] C. K. Li,[1] J. Lindl,[2] T. Ma,[2] A. Mackinnon,[2] A. Macphee,[2] M. J.-E. Manuel,[1] D. Meyerhofer,[5] J. Moody,[2] E. Moses,[2] S. Nagel,[2] A. Nikroo,[6] A. Pak,[2] T. Parham,[2] R. D. Petrasso,[1] R. Prasad,[2] J. Ralph,[2] M. Rosen,[2] J. S. Ross,[2] T. C. Sangster,[5] S. Sepke,[2] N. Sinenian,[1] H. W. Sio,[1] B. Spears,[2] P. Springer,[2] R. Tommasini,[2] R. Town,[2] S. Weber,[2] D. Wilson,[4] and R. Zacharias[2]

[1)] *Plasma Science and Fusion Center, Massachusetts Institute of Technology, Cambridge, MA 02139, USA*

[2)] *Lawrence Livermore National Laboratory, Livermore, CA 94550, USA*

[3)] *Sandia National Laboratory, Albuquerque, NM 87185, USA*

[4)] *Los Alamos National Laboratory, Los Alamos, NM 87545, USA*

[5)] *Laboratory for Laser Energetics, University of Rochester, Rochester, NY 14623, USA*

[6)] *General Atomics, San Diego, CA 92186, USA*

(Dated: 15 October 2014)

The effects of shock dynamics on compressibility of indirect-drive ignition-scale surrogate implosions, CH shells filled with D^3He gas, have been studied using charged-particle spectroscopy. Spectral measurements of D^3He protons produced at the shock-bang time probe the shock dynamics and in-flight characteristics of an implosion. The proton shock yield is found to vary by over an order of magnitude. A simple model relates the observed yield to incipient hot-spot adiabat, suggesting that implosions with rapid radiation-power increase during the main drive pulse may have a 2× higher hot-spot adiabat, potentially reducing compressibility. A self-consistent 1-D implosion model was used to infer the areal density (ρR) and the shell center-of-mass radius (R_{cm}) from the downshift of the shock-produced D^3He protons. The observed ρR at shock-bang time is substantially higher for implosions where the laser drive is on until near the compression bang time ('short-coast'), while longer-coasting implosions have lower ρR. This corresponds to a much larger temporal difference between the shock- and compression-bang time in the long-coast implosions ($\sim$ 800ps) than in the short-coast ($\sim$ 400ps); this will be verified with a future direct bang-time diagnostic. This model-inferred differential bang time contradicts radiation-hydrodynamic simulations, which predict constant $700 - 800$ps differential independent of coasting time; this result is potentially explained by uncertainties in modeling late-time ablation drive on the capsule. In an ignition experiment, an earlier shock-bang time resulting in an earlier onset of shell deceleration, potentially reducing compression and thus fuel ρR.

PACS numbers: 52.57.-z, 52.35.Tc, 52.70.Nc

I. INTRODUCTION

In the inertial confinement approach to laboratory fusion,[1,2] substantial compression of the fuel is required in MJ-scale implosions such as those at the National Ignition Facility (NIF)[3]. A spherical convergence ratio (ratio of initial to final radius) of ~ 35 is necessary to achieve the conditions required for ignition and energy gain.[2]

While ignition experiments at the NIF use targets with cryogenic layers of DT fuel, numerous surrogate implosions have been conducted where the layer of DT ice is replaced with a surrogate mass of ablator material (CH). The hydrodynamics before deceleration are nearly identical for the cryogenic layered and surrogate implosions,[4] enabling complementary studies and diagnostics of implosion dynamics, such as symmetry[5,6] and velocity.[7,8] One of the main objectives of using these surrogate implosions is to characterize the implosion at various stages to benchmark radiation-hydrodynamics simulations.[4,9–11]

In an implosion, a series of spherically converging shocks are launched with increasing strength. These shocks eventually coalesce at the capsule's inner edge and then converge at the center of the implosion. The final shock 'rebounds' and briefly creates high-ion-temperature conditions at the center of the implosion.

[a)] Electronic mail: zylstra@mit.edu

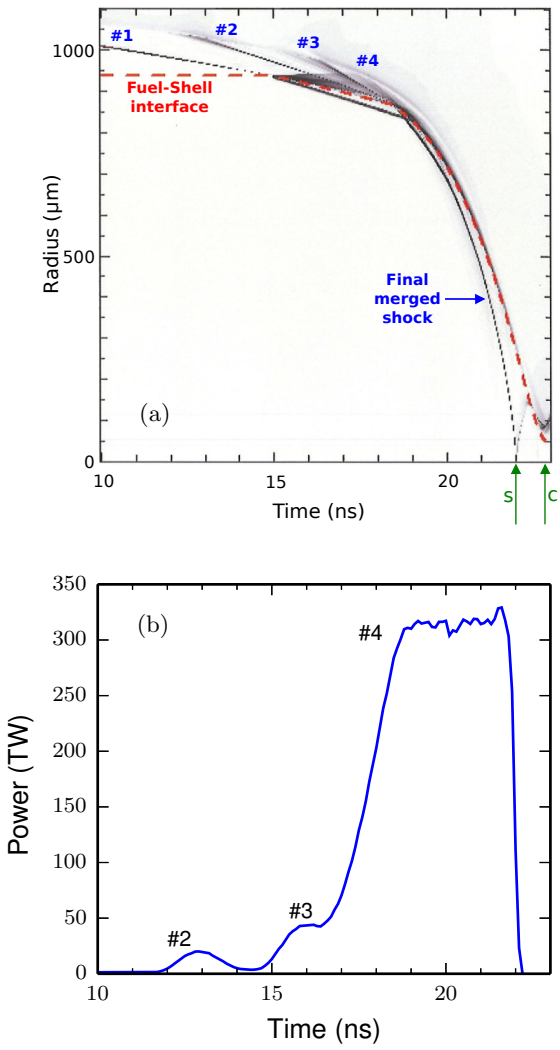

FIG. 1: NIF surrogate shot N120408-001-999 (CH shell with D^3He gas, see Fig. 3). **(a)** Simulated shock trajectory, visualized as the pressure gradient $|(1/P)dP/dr|$ where black indicates a higher value. The shock plot shows the four shocks launched into the shell, which merge to form the final shock that travels to the center where it rebounds, increasing the temperature and density, creating the shock burn at 22.03 ns. The compression bang time is at 22.83ns. Simulated shock (s) and compression (c) bang times are indicated by the arrows. **(b)** Laser pulse (foot before 10 ns not shown). In the drive, the pickets at ~ 13 and ~ 16 ns launch the 2^{nd} and 3^{rd} shocks respectively, with the 4^{th} launched by the rise to peak power.

In the case of surrogate implosions at NIF with a D^3He gas fill, this ion temperature is high enough to produce energetic protons via the fusion reaction:

$$D + {}^3He \rightarrow \alpha\ (3.67\ \text{MeV}) + p\ (14.7\ \text{MeV}). \quad (1)$$

For surrogate implosions at the NIF, this 'shock burn' occurs several hundred ps before the main compression

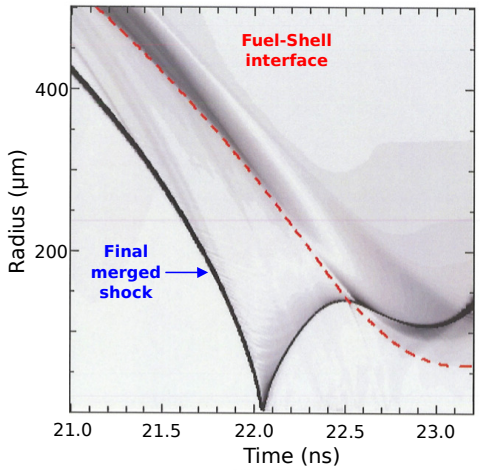

FIG. 2: Shock trajectory through rebound, shock burn, and compression phases, for the same simulation as Fig. 1a.

burn, and is approximately concurrent with peak shell implosion velocity. This is shown for a typical surrogate implosion in Fig. 1 using the radiation-hydrodynamics code HYDRA[11], where the simulated shock trajectories for the four launched shocks and final merged shock are shown in Fig. 1a as contours of the normalized pressure gradient $|(1/P)dP/dr|$. The laser pulse is shown in Fig. 1b, a detailed view of the shock dynamics around the shock-bang time and compression-bang time is shown in Fig. 2, and the capsule dimensions are shown in Fig. 3.

After the final merged shock rebounds at ~ 22 ns the shock burn occurs over ~ 100 ps, producing energetic D^3He protons (Eq. 1). These escaping protons are used to probe the in-flight characteristics of the shell at a radius of $\sim 250\mu$m.

D^3He proton spectroscopy is a well-developed technique for diagnosing inertial fusion implosions[12–16] at the OMEGA laser facility[17] and now at the NIF.[18,19] A typical measured D^3He proton spectrum is shown in Fig. 4. The protons have been energy downshifted to ~ 11.5

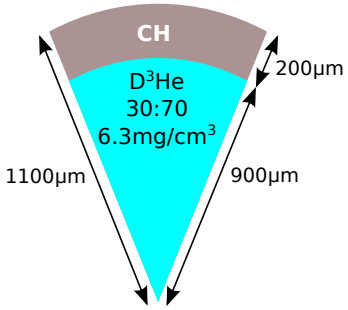

FIG. 3: Typical NIF surrogate capsule (see Table II for more information). The plastic shell ($\rho = 1.08$ g/cm^3) is filled with 30:70 atomic D and ^{3}He fuel.

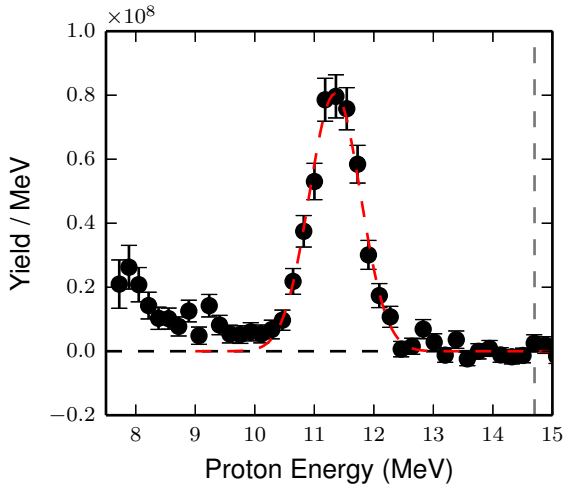

FIG. 4: Sample D^3He proton spectrum from NIF shot N101004-002-999, measured on the equator (DIM 90-78 Wedge Range Filter (WRF) #1) after hohlraum correction. The D^3He average birth energy of 14.7 MeV is shown by the vertical dashed line. The red dashed line is a Gaussian fit to the spectrum. Surplus protons at low energy, $\sim 8-9$ MeV, are due to the onset of compression burn. More details are given in Appendix A

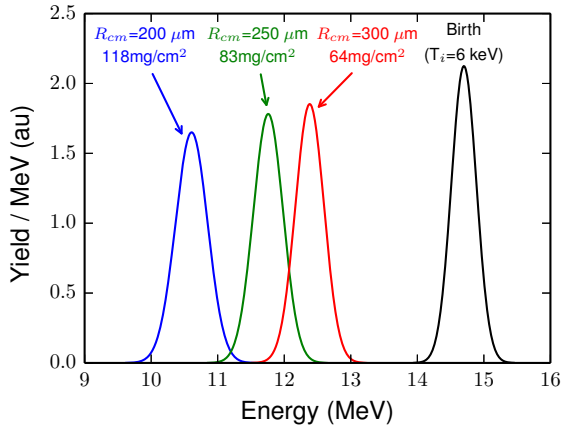

FIG. 5: For illustration, modeled D^3He proton spectra at birth (black) downshifted through 64 (red), 83 (green), and 118 (blue) mg/cm^2 of ρR are shown. The downshifts are calculated with a 1-D self-consistent model. Values of the shell $R_{\rm cm}$ associated with each spectrum are also shown.

MeV from the birth energy of 14.7 MeV. The downshift is caused by Coulomb collisions with the imploding plasma electrons[20], and the observed downshift can be related to the implosion areal density (ρR) using a charged-particle stopping theory[21]. The shock yield observed (8.7×10^7) is related to the final merged shock strength[16,22]. The center-of-mass radius ($R_{\rm cm}$) of the imploding shell is inferred in addition to ρR using 1-D modeling discussed in Section II.

As a probe of the implosion shock dynamics, this technique is unique in that it probes the strength of the final merged shock when it hits and rebounds from the center of the implosion. This measurement is complementary to the shock-timing measurements of the shock velocity that use an interferometry technique,[23] which has been highly successful at understanding the shock dynamics in the shell for radii larger than $600-700\mu$m.[24–27] At smaller radii the interferometry measurements 'blank'. As a result, the interferometry measurement would not see any additional shocks launched later in the implosion after the blanking, and does not probe the shock dynamics in the gas, when spherical convergence effects are significant; as the shock strength increases with convergence,[22] non-hydrodynamic behavior may become important.[28,29]

The paper is organized as follows: an implosion model for interpreting the spectral results is presented in Section II. Section III gives an overview of the experiments, Section IV discusses a down-selection of the available shots, which are analyzed in Section V to study the shock dynamics, Section VI interprets the results and their relevance to implosion compressibility, and the paper is concluded in Section VII.

II. IMPLOSION MODEL

The D^3He protons slow down monotonically as they traverse any material between the source and spectrometer. The measured proton downshift is directly related to the implosion ρR at the time of shock burn. This is illustrated in Fig. 5, which shows the birth spectrum plus modeled spectra for several values of the shell center-of-mass radius ($R_{\rm cm}$) and ρR using the model described in this section. These values span the typical range at shock-bang time in NIF implosions.

To relate the measured D^3He proton spectrum to the implosion conditions, a model involving charged-particle stopping theory[21] is required. The simplest 0-D model is to take a single characteristic plasma composition, density, and electron temperature from a simulation or an estimate, and then use a stopping power theory to calculate dE/dr. This works well for OMEGA implosions where the dense shell dominates slowing[15], but for ignition-scale surrogate implosions being conducted at the NIF a significant fraction of proton slowing during the shock burn occurs in the fuel and ablated material. These plasmas have much lower density and higher temperature than the dense shell, so a single choice of plasma conditions cannot accurately describe the entire system.

This necessitates a 1-D self-consistent model, which is constructed using initial target conditions and assumptions about in-flight plasma conditions to specify the density and temperature profiles of the implosion. As the

shell converges, the ρR increases and the energy of emitted protons decreases. The shell center-of-mass radius R_{cm} is taken as a free parameter, and thus is varied to obtain $\rho R(R_{cm})$ with $\rho R \equiv \int_0^\infty \rho(r)dr$. Similarly, the energy of protons escaping the implosion is calculated as a function of R_{cm} by

$$E_p(R_{cm}) = E_0 - \int_0^\infty \frac{dE}{dr}(r, R_{cm})\ dr, \tag{2}$$

where E_0 is the average birth energy of the protons. The charged-particle stopping power dE/dr depends on plasma conditions specified by the model and thus on both r and R_{cm}. The Li-Petrasso theory[21] is used in this work.

The initial capsule conditions are used as a model input: the shell material, inner and outer radii, and gas fill (composition and initial pressure). Fig. 3 illustrates the typical capsule dimensions and gas fill. The model makes assumptions about the in-flight characteristics of the implosion, informed by data when available or 1-D HYDRA[11] simulations: temperature in the fuel, shell, and ablated mass, the thickness[30] and mass remaining of the shell, and an ablated mass profile.

With the initial conditions and in-flight assumptions, the gas density and ρR scale with R_{cm} as

$$\rho_{\rm gas} = \rho_{0,\rm gas}\left(\frac{R_i}{R_{cm} - \Delta R_s/2}\right)^3, \tag{3}$$

$$\rho R_{\rm gas} = \rho_{\rm gas}(R_{cm} - \Delta R_s/2), \tag{4}$$

where $\rho_{0,gas}$ is the initial gas density, R_i is the initial inner shell radius, and ΔR_s is the in-flight shell thickness.

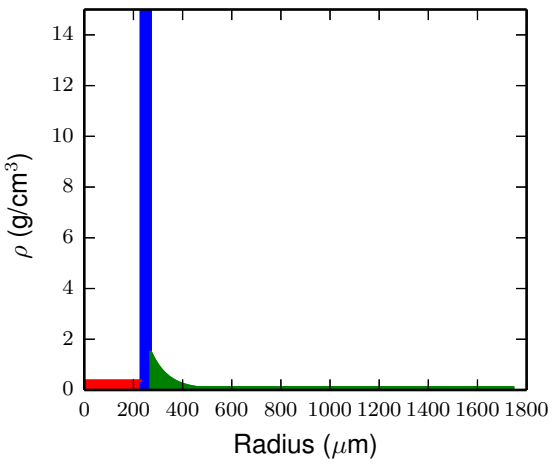

FIG. 6: Density profile used in the 1-D model at $R_{\rm cm} = 250$ μm. This center-of-mass shell radius is typical for NIF shots at shock-bang time. The gas material is shown in red (8 mg/cm^2), the shell is shown in blue (53 mg/cm^2), and the ablated mass is in green (23 mg/cm^2).

Similarly, the shell conditions are given by

$$\rho_{\rm shell} = \frac{M_{rem}\ \rho_{0,\rm shell}\ (R_o^3 - R_i^3)}{(R_{cm} + \Delta R_s/2)^3 - (R_{cm} - \Delta R_s/2)^3}, \tag{5}$$

$$\rho R_{\rm shell} = \rho_{\rm shell}\Delta R_s, \tag{6}$$

where $\rho_{0,\rm shell}$ is the initial shell density, M_{rem} is the remaining mass fraction, and R_o and R_i are respectively the initial outer and inner radii of the shell.

The ablated mass profile is specified by

$$\rho(r) = \begin{cases} \rho_{\rm max} \times e^{-(r-r_0)/\lambda} & \text{if } r_0 \le r \le r_1 \\ \rho_{\rm min} & \text{if } r_1 \le r \le r_2 \end{cases}, \tag{7}$$

where $r_0 = R_{cm} + \Delta R_s/2$ is the outer radius of the imploding shell, $\rho_{\rm max}$ and $\rho_{\rm min}$ are the maximum and minimum densities of ablated material, and λ is a characteristic scale length in the ablation region. The radius r_1 is determined by requiring continuity of the ablated mass density profile as described by Eq. 7, and r_2 is determined by conservation of total mass. The values of ρ_{max}, ρ_{min}, and λ are model assumptions. The areal

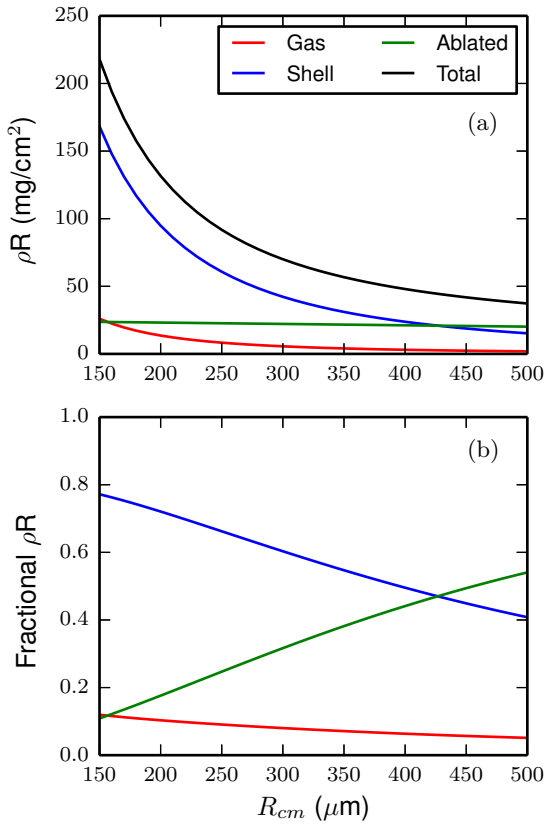

FIG. 7: ρR components (gas, shell, and ablated material) as a function of R_{cm} for typical model parameters. The results are plotted as absolute ρR **(a)**, and normalized to the total **(b)**.

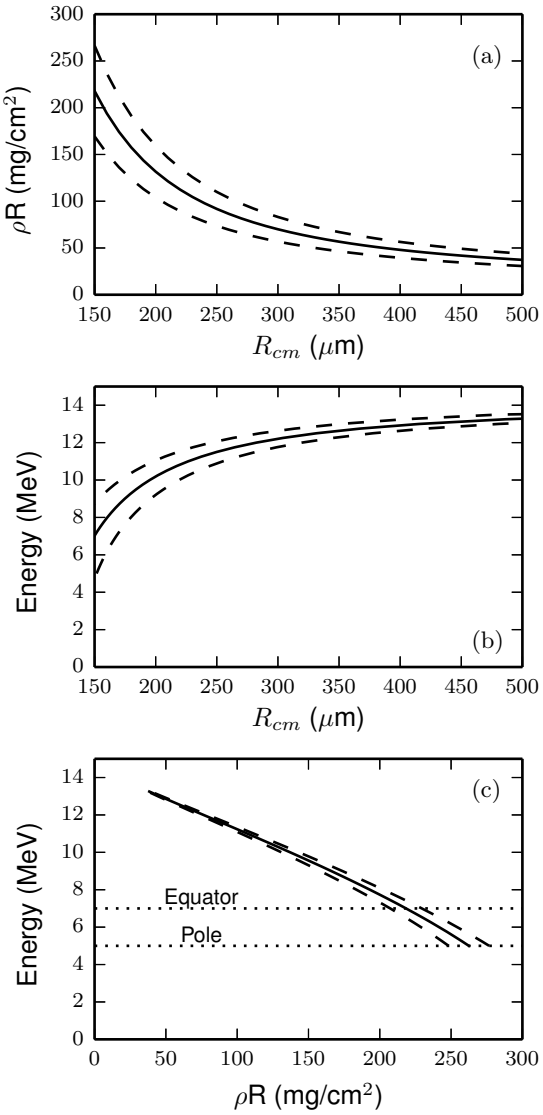

FIG. 8: **(a)** Modeled ρR vs R_{cm}, **(b)** Average energy of emitted protons vs R_{cm}, and **(c)** Average energy of emitted protons vs ρR. The dashed curves indicate the uncertainties in the modeling. The instrumental lower cutoffs are shown in (c) by dotted lines at 5 MeV (pole), and $7-8$ MeV for the equator, increased due to the energy loss in the hohlraum wall (see Fig. 10).

density of ablated material is

$$\rho R_{\rm abl} = \int_{r_0}^{r_2} \rho(r) dr = \rho_{\rm max}\lambda\left[1 - e^{-(r_1-r_0)/\lambda}\right] + (r_2 - r_1)\rho_{\rm min}. \quad (8)$$

An example of the modeled density profile is shown for $R_{\rm cm} = 250$ μm in Fig. 6. The components of ρR, e.g. Eqs 4, 6, and 8, are calculated as functions of R_{cm} both in absolute values of mg/cm^2 and also as fractions of the total ρR (Fig. 7). The gas and shell ρR depend strongly on convergence (Eqs 4 and 6) while the ablated material ρR only increases modestly as R_{cm} decreases. Thus for $R_{cm} \sim 200 - 300\mu$m, the shell ρR will dominate with $60 - 70\%$ of the total ρR.

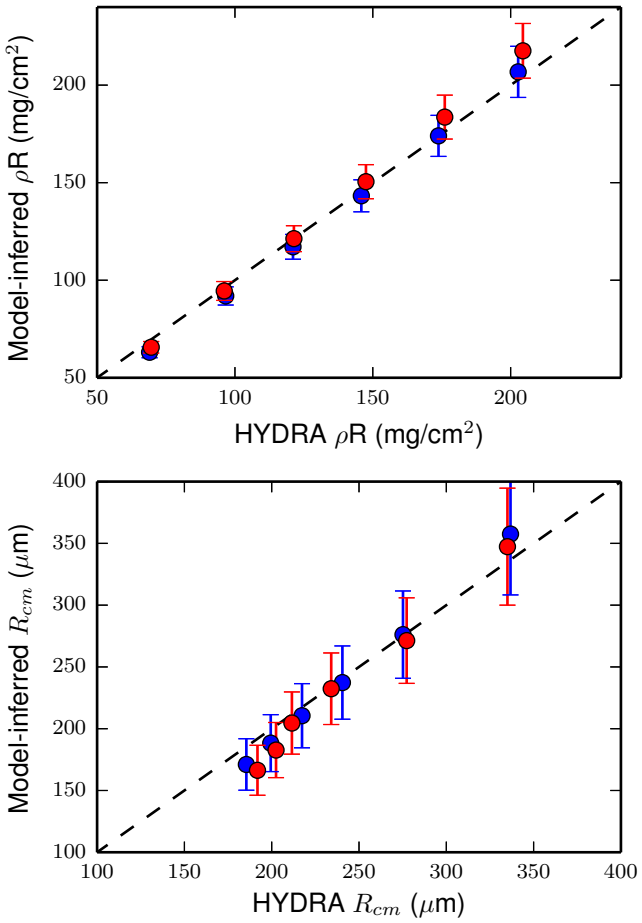

FIG. 9: Comparison between model-inferred ρR (top) and R_{cm} (bottom) using synthetic emitted proton energies from HYDRA simulations, compared to values directly extracted from the simulation. Six time snapshots are used from two simulations: nominal (blue) and high preheat (red).

The final result of the model is the relationships between the three quantities: R_{cm}, ρR, and emitted proton energy (E_p). For the typical parameters, the model produces the curves shown in Fig 8. For completeness we show the ρR vs R_{cm}, E_p vs R_{cm}, and finally the ρR vs E_p curves. Thus the measured quantity (E_p) can be converted directly into ρR and R_{cm} using these relationships.

Each quantity used in the model has an associated error bar, which is used to calculate the uncertainty in the inferred quantities. This is done by an in-line sensitivity analysis to variations in the input quantities. For details

of the model inputs and uncertainties, see Appendix C. As the model uncertainties are assumed to be uncorrelated, they are added in quadrature. Any uncertainties in the proton measurement are propagated in quadrature with the model uncertainties. Uncertainties are shown in Fig. 8 by the dashed curves.

This model can be validated against radiation-hydrodynamic simulations using HYDRA. In the simulation, full profiles of hydrodynamic variables (density and temperature) are output at several times. The emitted D^3He proton energy is then calculated using the full profiles. The calculated energy is then analyzed with the model, and the model-inferred values for ρR and R_{cm} can be compared to known values directly extracted from the simulation. This is shown in Fig. 9 for two different simulations of shot N120408, where six snapshots are used from each simulation corresponding to varying ρR and R_{cm}. The blue points correspond to a nominal simulation, while the red points are a simulation with significant preheat (changing the implosion trajectory and plasma conditions in the shell). Typical model error bars are shown. The chosen times span the typical range of shock ρR and R_{cm} observed. The model's agreement with both simulations of shot N120408, with significantly different plasma conditions between the simulations, shows that the uncertainties used in the model cover the range of expected variation in plasma conditions. This comparison shows excellent agreement between the simulation and model, demonstrating the model's fidelity as an analysis tool.

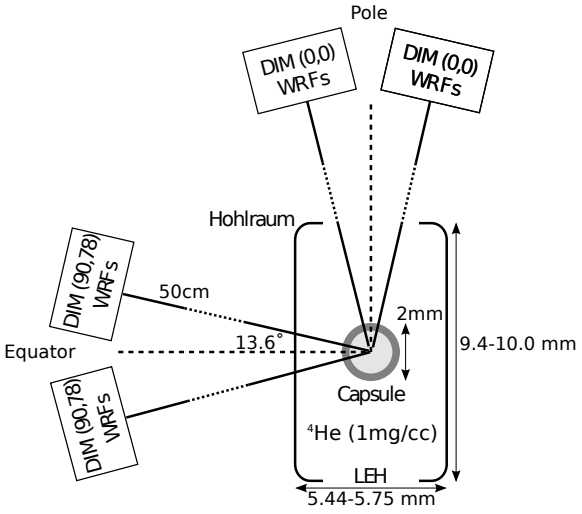

FIG. 10: WRF setup on the NIF. Compact WRF proton spectrometers are placed at $\pm 13.6°$ to the DIM axis on both the pole [DIM (0,0)] and equator [DIM (90,78)].

III. NIF EXPERIMENTS

The compact Wedge Range Filter (WRF) proton spectrometers[18,31,32] have been used at the NIF since 2009. Between 1 and 4 spectrometers are fielded on the polar (0-0) and equatorial (90-78) diagnostic manipulators (DIMs)[33]. Each WRF provides a complete spectral measurement of the D^3He protons, from which yield, ρR, and R_{cm} are inferred.

WRF proton spectrometers have been used on a total of 85 surrogate D^3He gas-filled indirect-drive implosions on the NIF, forming the basis of this work. For these experiments, the total laser energy varied in the range $0.9 - 1.9$ MJ, and the peak laser power was between $243 - 522$ TW. Gas-filled Au or depleted U (DU) hohlraums were used in these experiments. The hohlraum width was 5.44mm ('544' geometry) or 5.75mm ('575' geometry) with varying lengths in the range of $9 - 10$mm. Details of the experimental geometry are conceptually shown in Fig. 10. Spectra measured on the equator must be corrected for energy loss in the hohlraum wall, see Appendix B.

The capsules were primarily CH with an outer radius varying from 1087 to 1169 μm and thickness from 188 to 231 μm. Si and Ge dopants are used within the shell. The gas fill was typically a 30:70 atomic mixture of D and ^{3}He at an initial gas density of 6.3 mg/cm^3. Each of these parameters is used in the ρR modeling described in the previous section (also see Fig. 3).

The complete dataset is shown in Fig. 11. Within a DIM, multiple WRFs are averaged when available to reduce random and statistical errors; the weighted mean and resulting uncertainty are shown. The measured ρR is shown in Fig. 11a. The random/statistical errors associated with the ρR values are dominated by the larger systematic and model uncertainties (see Sec. II and Appendix C). Many of the shots have asymmetries between the pole and equator: these asymmetries are discussed in a separate publication[19]. Overall the ρR typically varies between $70 - 110$ mg/cm^2. The most notable set of outliers are the implosions with ρR in the range of $160 - 170$ mg/cm^2 measured on DIM 90-78. The distinguishing feature for these implosions is that they were conducted as part of a series of low-power short-coast implosions.

The proton shock-yield data for the entire dataset is shown in Fig. 11b. Only data from the equator (DIM 90-78) is shown. This is because the polar yield data is affected by transverse electromagnetic field structures at the LEH, which can cause deflections and thus a reduction in the apparent yield observed by the WRFs on the pole[34–36]. A significant shot-to-shot yield variation is observed, i.e. $(1 - 35) \times 10^7$. Fundamentally the large variability is due to the extreme temperature sensitivity of the D^3He reaction, which makes the shock-proton yield very sensitive to the final shock strength.[16,22]

Finally, the inferred shell center-of-mass radius (R_{cm}) is shown in Fig. 11c. According to this analysis, the shell is typically at a radius of $250 - 300$ μm at the shock-

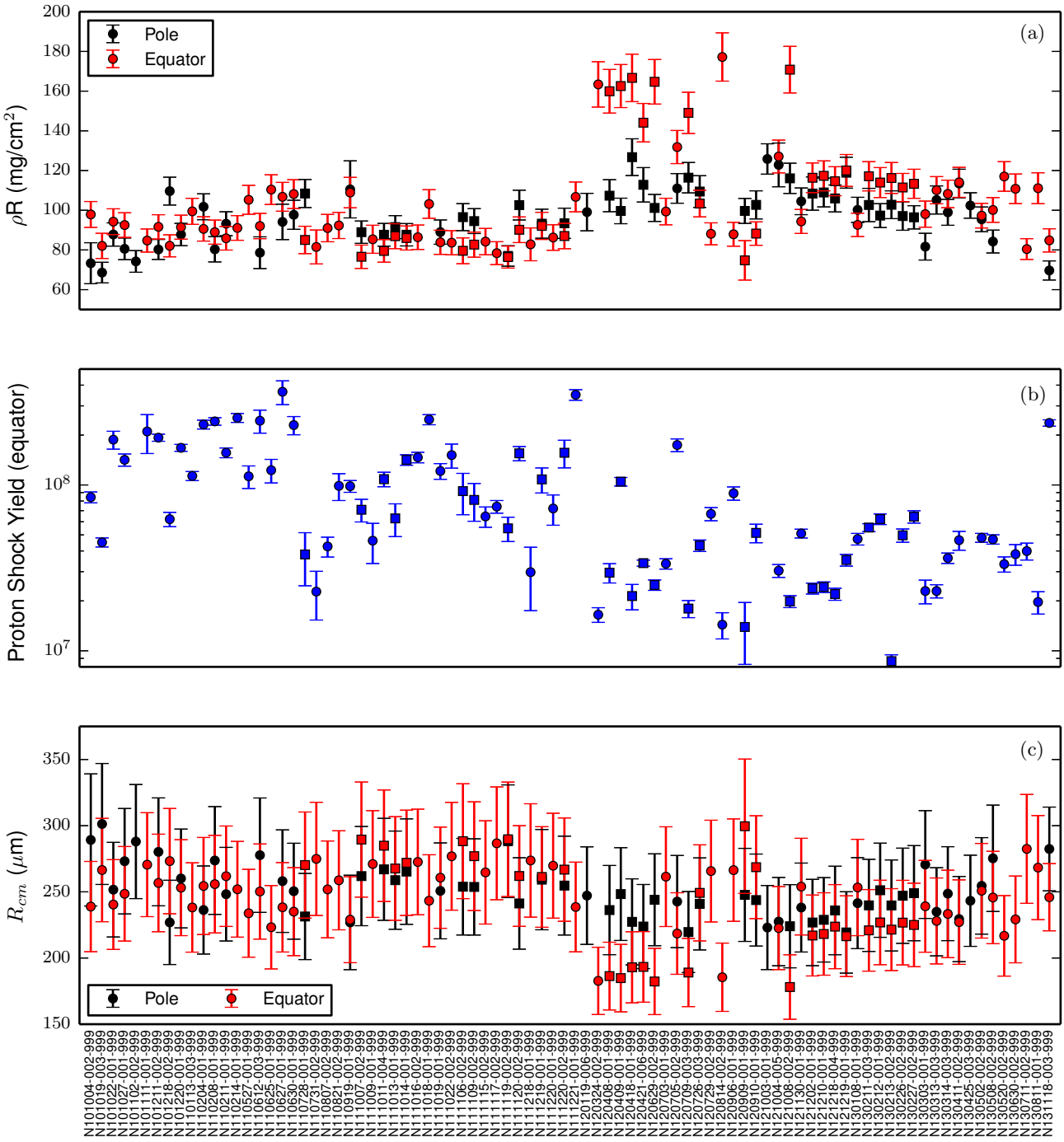

FIG. 11: WRF data for all surrogate implosions. (a) Shock ρR data. When available both polar (DIM 0-0) and equatorial data (DIM 90-78) are shown. (b) Shock proton yield measured by WRFs on DIM 90-78. (c) Center-of-mass shell radius (R_{cm}) plotted as average values for both pole (DIM 0-0) and equator (DIM 90-78).

bang time. In the high ρR cases, the inferred R_{cm} is as low as ~ 190 μm. However, the error bars are large, typically $\pm 25-30$ μm, caused by the model uncertainties (described in Section II).

IV. DATA DOWN-SELECTION

Due to the large shot-to-shot parameter variations during the NIF campaigns, it is necessary to select a subset of implosions with similar overall conditions for detailed analysis. We perform this down-selection using the fol-

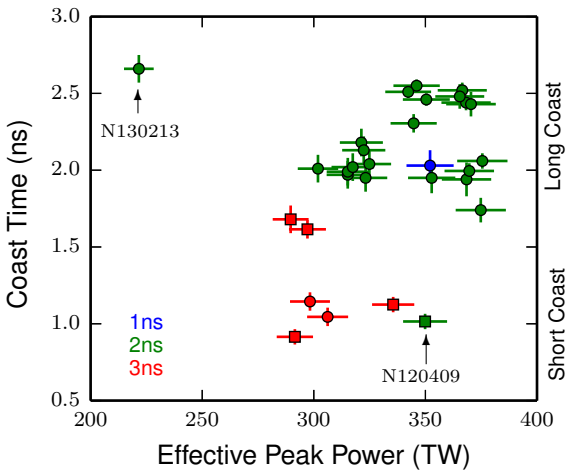

FIG. 12: Coast time and peak power of down-selected experiments. With a few exceptions, implosions have been conducted at low-power, short-coast (∼ 300TW, ∼1ns) conditions or high-power, long-coast (∼ 350TW, ∼2ns) conditions.

lowing criteria:

1. Standard capsules (CH with D^3He fill, see Fig. 3)
2. 5.75mm diameter hohlraums
3. WRF data available on both pole and equator
4. Low-adiabat ('4-shock') pulse shapes

This reduces the number of shots to 30. Criterion #3 is required to allow for modeling of the observed ρR asymmetries (see Fig. 11a and Ref. 19) and determining of

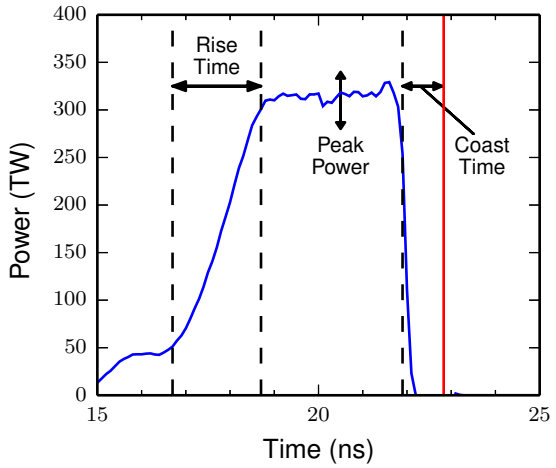

FIG. 13: Relevant variables of the laser pulse: rise time, peak power, and coast time. In this case, the rise time is 2ns, the peak incident power is 300TW, and the coasting time is 0.9ns (short-coast, while long-coast is ∼2ns). The bang time is indicated by the red line.

average values for ρR and R_{cm}. Shots selected via these criteria are used in subsequent analysis and are denoted in Fig. 11 by square markers.

V. SHOCK DYNAMICS

The shock dynamics of the down-selected set of 30 implosions can now be explored. The observations indicate that the shock dynamics are most sensitive to the peak power of the laser drive, the coasting time of the implosion, and the rise time of the main laser pulse, see Fig. 13.

Since the effective drive experienced by the capsule depends on the absorption of the incident laser light and the effectiveness of conversion to x rays, we add 25TW to the actual laser power for DU hohlraums to account for the latter, and then multiply by the observed absorption fraction to account for the former. The 25TW effective increase in power is based upon measured enhancements in radiation temperature when using DU hohlraums[37]. This gives an 'effective peak power' which is used in this work. The coasting time of an implosion is defined as the difference between the end of the laser drive and the measured compression bang time. The rise times used in these experiments are discrete, with design values of 1, 2, or 3 ns.

With these definitions, the main observables (average ρR and shock yield) are plotted versus the effective peak power, coasting time, and rise time. The data are shown in Fig. 14. To eliminate the effect of low-mode asymmetries observed in these implosions, this analysis uses an average ρR obtained from a fit to the polar and equatorial ρR data (see Appendix D and Ref. 19). The different rise times used are differentiated by marker color. Furthermore, the hohlraum material is specified by marker shape: square markers for DU and circular markers for Au hohlraums.

The distribution of implosion parameters used (peak power, coast time, and rise time) is illustrated by Fig. 12. With a few exceptions, the experiments fall into two groups:

1. Low-power (∼ 275−325 TW), short-coast (∼ 1−1.5 ns), slow-rise (3ns)
2. High-power (∼ 325−375 TW), long-coast (∼ 2−2.5 ns), fast-rise (1 or 2 ns)

Since these two groups are diametrically opposed in all three parameters disentangling their effects requires using a few select implosions that do not fall into these groups. For the rise time a set of three implosions was conducted where only the rise time was varied, significantly aiding this interpretation.

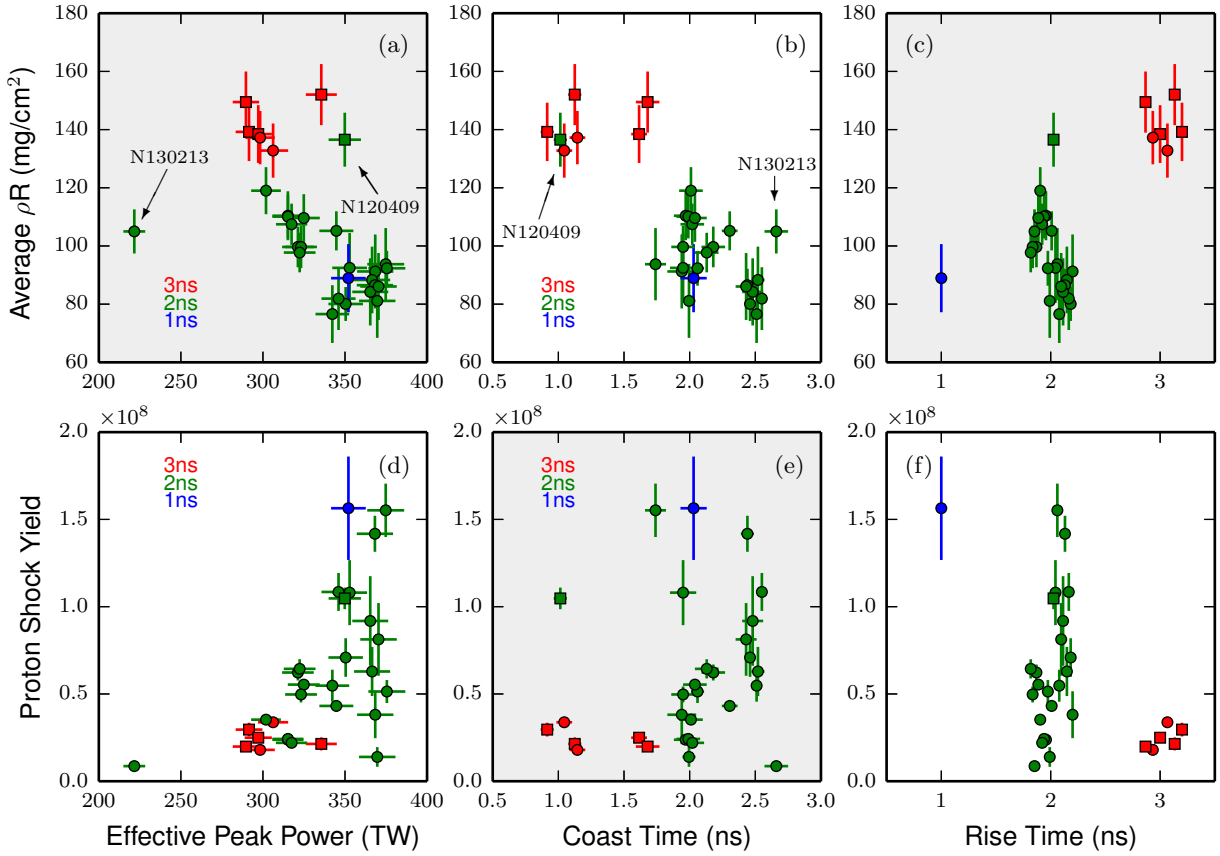

FIG. 14: Shock ρR and yield data [ρR (a-c) and Y_p (d-f)] versus effective peak power (a,d), coast time (b,e), and rise time (c,f). For the rise time, points are artificially displaced for clarity around the values 1, 2, or 3 ns (see c,f). Rise time is further specified by point color: 1ns (blue), 2ns (green), and 3ns (red) to improve clarity in the power and coast time plots. Additionally, Au-wall hohlraums are denoted by circular markers, and DU-wall hohlraums by square markers.

A. Shock yield interpretation

First, the interpretation of the shock-yield data can be aided by a set of three shots conducted in which only the rise time was varied. This data is shown in Fig. 15a. The faster rise pulse shapes clearly create higher shock yields. This is consistent with the data in Fig. 14f.

Conversely, the coast time (Fig. 14e) has no clear effect on the shock yield, since short- and long- coast times have data with both high- and low- shock yield.

For the peak power, the data in Fig. 14d suggests a trend, where lower peak power creates a weaker shock. This is intuitive and consistent with the fact that all low power ($\lesssim$ 300 TW) shots have low yield, but at higher power the shock yield displays significant variation.

We conclude that the faster-rise pulses create shock yields $2-3\times$ higher (Fig 14f and 15) with other variables constant, and that increasing the peak power may increase the shock yield. We note that the shock yield varies by approximately $15\times$ over the dataset, indicating substantial variation in shock strength.

B. ρR interpretation

Two shots that do not fit into the overall implosion parameter grouping are essential to understanding the data: N120409, which was a high-power short-coast shot, and N130213 which was a low-power long-coast shot. These two are specifically annotated in Fig. 12 and Fig. 14a-b.

Fig. 14a plots the shock ρR versus effective peak power. Neglecting the results from shots N120409 and N130213, the data show an anti-correlated trend between ρR and peak power. However, shots N120409 and N130213 clearly suggest that this trend is due to the preponderance of high-power long-coast and low-power short-coast implosions. For the coasting, a clear trend is observed in Fig. 14b, including both N120409 and N130213 where large coast times generate significantly lower shock ρR than short-coast implosions.

In Fig. 15 the set of three shots with a controlled rise time show no change in shock ρR as the rise time is varied. This demonstrates that the rise time has no effect on the shock ρR; the apparent trend in Fig. 14c is

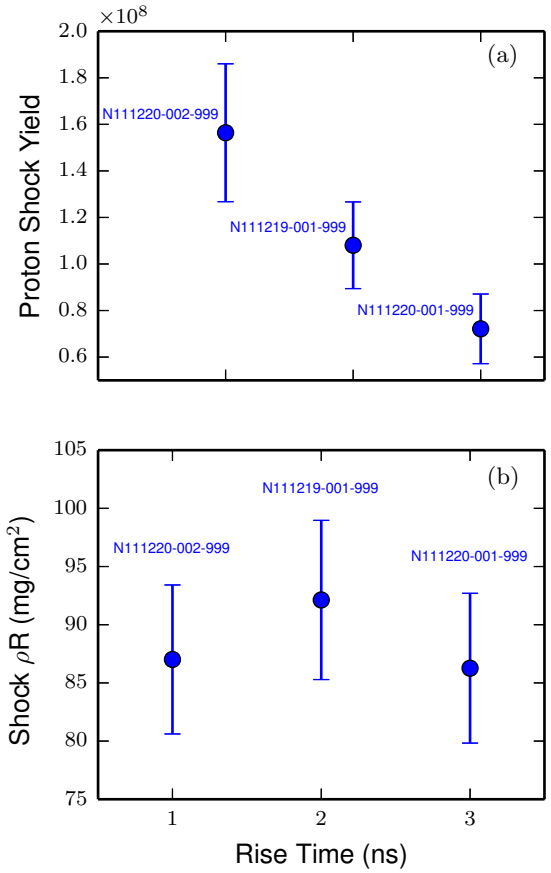

FIG. 15: Shock yield (a) and ρR (b) versus rise time for a set of three shots where only the rise time was varied.

due to the low coasting times in the 3ns rise implosions.

C. Estimated shock-bang time

The dependence between shock ρR and coast time can be further investigated. Fundamentally, the ρR is mainly determined by the shell R_{cm} at the shock-bang time (see Section II).

On many of these shots, simultaneous x-ray radiographs of the implosion trajectory were obtained[7,8,38], and from the x-ray radiographs, $R_{cm}(t)$ is determined near the shock-bang time. Presently the shock-bang time is not directly measured, but the combination of the trajectory measurement and WRF-inferred R_{cm} from shock-produced protons can be used to estimate the shock-bang time. This technique is shown in Fig. 16.

From the x-ray data we know the shell velocity at $R_{cm} = 200$ or 300 μm. The absolute timing uncertainty of the x-ray measurement relative to compression bang time is ± 50 ps. We know that the compression-bang time uncertainty is typically ± 50 ps or better. From this information, combined with the x-ray and proton data, a shock-bang time can be determined relative to

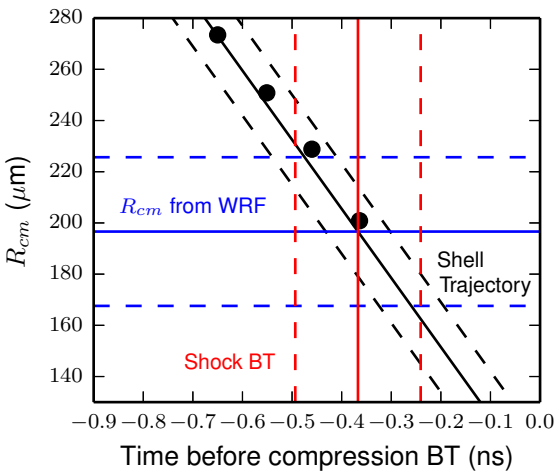

FIG. 16: R_{cm} versus time before compression-bang time for shot N120408-001-999. As the shell trajectory (black) and R_{cm} (blue) are determined from x-ray radiography and WRF proton spectroscopy, respectively, the shock-bang time (red) can be estimated. Error bars are shown by dashed lines. For this shot, $\Delta_{BT} = 0.34 \pm 0.13$ ns.

compression-bang time: $\Delta_{BT} \equiv t_{shock} - t_{comp}$, to remove any variation in absolute implosion timing. The uncertainty in R_{cm} from this analysis is used to determine the uncertainty in the shock-bang time in addition to the uncertainty in timing of the x-ray measurement and shell velocity.

The shock-bang time is estimated for a set of 14 experiments (a subset of Fig. 14) where x-ray radiography is available, and shown in Fig. 17. The estimated bang time difference ranges from $\sim 0.4-0.8$ ns. The displayed error bars represent random (shot-to-shot) uncertainties, while the larger systematic uncertainty is $\pm$0.11ns.

For this data, a clear trend is shown where the long-coast implosions have substantially larger differential bang time (more negative Δ_{BT}) than the short-coast shots.

Simulations of Δ_{BT} exist for five of these shots (one of which, N120408-001-999, was simulated and presented earlier in Figs. 1 and 2); these simulations are also shown in Fig. 17. The simulations predict a nearly constant Δ_{BT} of $\sim -(0.7-0.8)$ns while the data show a clear trend where long-coast implosions have a larger differential bang time.

VI. INTERPRETATION

A. Coasting

The data indicate that the shock-bang time occurs earlier relative to the main compression burn in long-coast implosions than in short-coast implosions. The interpre-

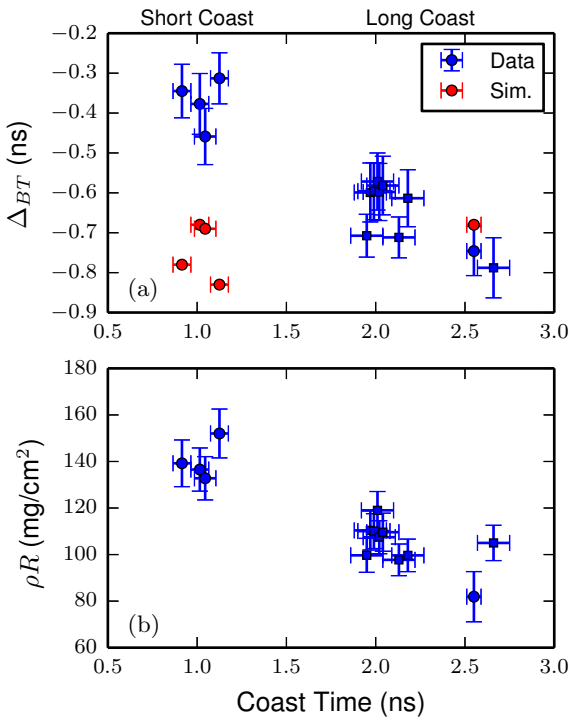

FIG. 17: **(a)** Estimated difference in time between shock and compression bang, contrasted to simulations, for 2DConA (square) and ConA (round) implosions, which were also probed with in-flight x-ray radiography. The two points at coasting time ~ 2.5ns show good agreement between the two experimental platforms. Uncertainties are random, with an additional ± 0.11ns systematic uncertainty. **(b)** ρR data for the same shots versus coast time. Higher ρR corresponds to higher convergence and thus smaller Δ_{BT}.

tation of this observation is that the imploding shell is at a larger radius (R_{cm}) during the shock bang for the long-coast implosions. This means that the final rebounding shock, which creates the shock bang, is either faster relative to the implosion velocity or launched earlier for the long-coast pulses.

The shock transit time in the gas (after break-out from the shell) is $\sim$ 4ns according to HYDRA simulations (see Fig. 1a). This can also be estimated using simple models. For example, using the Hugoniot conditions, a shock launched by 100 MBar of pressure at the ablation front propagates through the pre-compressed shell in approximately 450ps. This shock propagates through the density discontinuity at the inner surface of the shell[39] and spherically converges as a Guderley shock[22] through the initial gas, which takes an additional ~ 4.1 ns. However, at the time when the shock is launched into the gas, the sound speed in the shell $c = \sqrt{\gamma P/\rho}$ is quite low. For an ideal gas at 100MBar pressure and density of $\rho = 20$ g/cc, the speed of sound is only ~ 30 μm/ns (in the frame of the imploding shell). But since the inward shell fluid velocity at shock breakout is ~ 60 μm/ns and the shock velocity in the lab frame is ~ 150 μm/ns, the shock is already effectively decoupled from the driving piston of the ablation front. The coasting dynamics happen later in time and thus cannot directly affect the shock strength in this scenario.

The late-time drive will affect the implosion (shell) trajectory. If the implosion comes in late relative to the shock, the bang-time differential will increase. This could occur, for instance, due to in-flight decompression and deceleration of the shell if the ablation pressure decreases while the shell is still at a large radius. Since the data and simulations are discrepant for the short-coast implosions, this suggests that the late-time drive (during the last ns) is not well modeled in the simulation. This could be related to the drive degradation multipliers[40] not accurately reflecting the late-time drive, an uncertainty in radiation transport through the ablated shell material, or an uncertainty in the compressed ablator equation of state. Another possibility is that severe mix in the coasting implosions may truncate the compression burn, moving the apparent compression bang time earlier and decreasing Δ_{BT}.

One potential significance of an earlier shock-bang time is its implications for the deceleration phase of the implosion. Deceleration begins when the rebounding shock (as a heat wave) encounters the incoming shell. The rebound phase can also be calculated using Guderley's solution[22]. For a constant shock strength, an earlier shock-bang time means that the rebounding shock will hit the incoming shell at an earlier time (larger radius) and thus deceleration will begin earlier. This could reduce the compression and final ρR of the implosion. Interestingly, data in cryogenic implosions show $25-50\%$ higher ρR and higher inferred stagnation pressure for short-coast implosions[37,41]. This is consistent with this work's interpretation of the short-coast implosions where the shock dynamics is more amenable to high compression, i.e. later shock-bang time relative to compression.

B. Hot-spot adiabat

The significance of large variation in shock proton yield can be interpreted in the context of the shock dynamics and hot-spot adiabat. The initial heating of the low-density material at the center of the implosion is from the imploding and rebounding shock, which sets the incipient hot-spot adiabat prior to the onset of deceleration and subsequent PdV heating of the hot spot. The hot-spot adiabat can be roughly characterized as the ratio of its pressure to the Fermi pressure:

$$\alpha \equiv \frac{P}{P_f} = \frac{n_e k_B T_e + n_i k_B T_i}{\frac{(3\pi^2)^{2/3}\hbar^2}{5m_e} n_e^{5/3}}. \quad (9)$$

The shock preferentially heats ions over electrons[16] and in this Guderley model they are assumed to be uncoupled

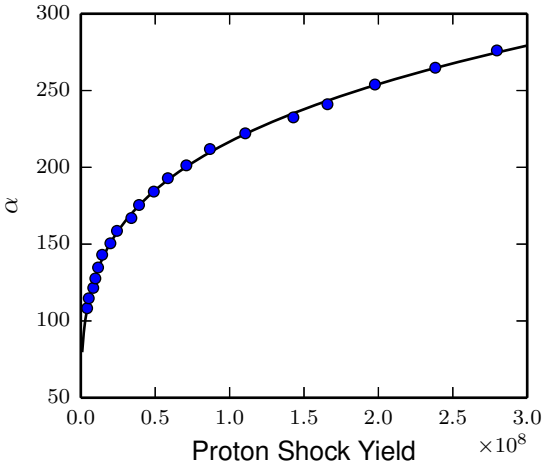

FIG. 18: Inferred hot-spot adiabat (α) versus proton shock yield using a Guderley model. Points are at values of ξ from $250-350$ (at intervals of 5) μm/ns$^{0.688}$. The solid curve is a power-law fit (see Eq. 10).

(τ_{ei} long compared to dynamical timescales)[42].

We can interpret the shock proton yield via a simple model based on the Gudelery spherically-imploding shock solution[16,22]. The Guderley model gives hydrodynamic profiles in a self-similar solution as a function of a single shock strength parameter, ξ. For a single choice of ξ, the D^{3}He yield (Y) is calculated from:

$$Y = \int f_D f_{3He} n_i^2 \langle \sigma v \rangle \; d^3 r dt, \tag{10}$$

where f_D and f_{3He} are the fuel ion fractions and $\langle \sigma v \rangle$ is the temperature-dependent fusion reactivity. A mass-weighted hot-spot adiabat is also calculated via Eq. 9, evaluated when the rebounding shock encounters the incoming shell material. The shock strength ξ is then varied to map out a relationship between the proton shock yield and hot-spot adiabat, and this relationship is well described by a power law:

$$\alpha = 2.10 Y^{0.247} + 16.4, \tag{11}$$

where the coefficients are from a fit to the model results. This relation is shown in Fig. 18.

Using this model, the adiabat can be determined from the yield and thus rise time (see Fig. 19). The hot-spot adiabat increases for faster rise times due to a stronger launched shock. This empirical result can be compared qualitatively to modeled hot-spot adiabats[43] for cryogenic implosions[37,44], in which a very similar trend is seen where α increases from ~ 100 to ~ 160 as the rise time decreases from 3 to 1 ns. The absolute values of α inferred for these surrogate implosions are expected to be higher than cryogenic implosions, since ablation of low-adiabat ice material in the latter decreases the hot-spot adiabat. Further modeling is required to directly relate

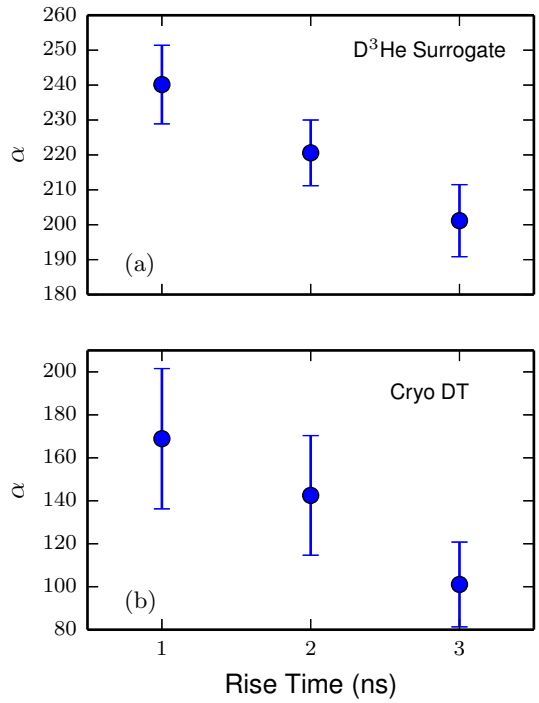

FIG. 19: **(a)** Modeled adiabat versus rise time for the same dataset as shown in Fig.15. **(b)** Modeled hot-spot adiabat in cryogenic implosions.

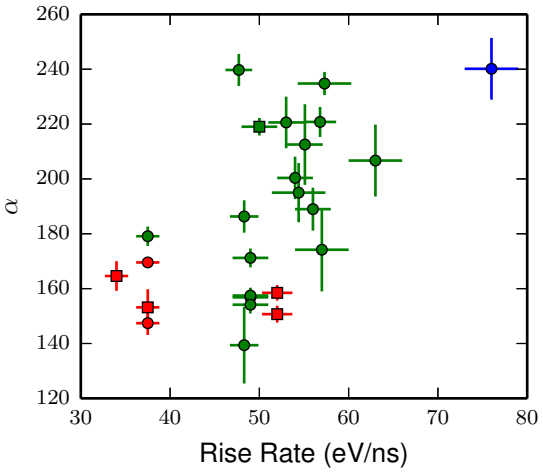

FIG. 20: Modeled adiabat versus rise rate for the same dataset as Fig.14d-f.

surrogate hot-spot adiabat to cryogenic hot-spot adiabat, but this is motivated by the lack of any other direct measurement of the hot-spot adiabat. Additionally, 3-D effects are expected to alter the inferred hot-spot adiabat in cryogenic experiments, so a better understanding of the incipient adiabat and hot-spot formation process may increase our understanding of these 3-D effects.

Inferred values of α as a function of measured

radiation-temperature rise rate are shown for the 30 downselected shots used in Fig. 20, analogous to Fig. 59 of Ref. 37. The factor of 10× variation in shock proton yield corresponds to ∼ 75% variation in α, as seen from the power 0.247 in Eq. 10. For the entire dataset (Fig. 11), a 35× min-max variation in shock yield is observed, corresponding to a ∼ 2.4× variation in α.

C. Kinetic Effects

The overall shock dynamics may be significantly affected by kinetic effects. For example, recent OMEGA experiments have shown experimental evidence for long ion-ion mean-free-path effects[28], enhanced diffusive mix[29], and temperature anomalies in shock-heated plasmas[45]. Relative to the OMEGA experiments of Refs 28, 29, and 45, in these experiments the initial gas density is ∼ 2× higher and the shock is weaker; at similar initial density to this work, an indirect-drive exploding pusher on NIF showed excellent agreement with simulation, suggesting a lack of kinetic effects[46]. Further experiments and computational studies are needed to assess whether kinetic effects could be playing a role in these observed anomalies in the NIF low-adiabat implosion shock dynamics.

VII. CONCLUSIONS AND FUTURE WORK

The shock dynamics of surrogate implosions at the NIF have been studied. From proton spectroscopy the shock ρR, proton yield, and shell radius at shock-bang time are determined using a simple self-consistent 1-D implosion model. The shock ρR data show dependence on the coasting time of the implosion, with short-coast implosions having higher shock ρR. The proton shock yield data show a clear dependence on the laser-pulse rise time, and possibly peak power. Using the inferred center-of-mass radius and in-flight x-ray radiography, a shock-bang time is estimated. The short-coast implosions are observed to have significantly smaller differences between the shock- and compression-bang times than the long-coast implosions. This could be due to uncertainties in modeling the late-time drive on the capsule, which is the primary difference between short- and long-coast experiments. An earlier shock-bang time in long-coast implosions could reduce compressibility due to an earlier onset of deceleration; in cryogenic implosions lower compression ρR is measured in long-coast implosions. Further, the large variation in shock yield indicates a variation in post-shock temperature and thus adiabat of the incipient hot-spot material. A model is introduced to relate the proton shock yield to adiabat; this analysis suggests an increase in hot-spot adiabat of up to 2× in fast-rise implosions, potentially reducing compressibility.

Future campaigns could be conducted to more systematically study the effect of coasting time, rise time, and peak power on shock dynamics, or to study the effect of hohlraum material (not addressed in this work). Implementation of a diagnostic for direct measurements of the shock-bang time, which is in progress[47], will be a direct and higher-precision diagnostic of the differential bang time. This new diagnostic will be used to further investigate the discrepancy observed in this work between the model-inferred differential bang time and radiation-hydrodynamics simulations (Fig. 17). The potential impact of kinetic effects on these observations should be studied with dedicated experiments (e.g. varying the gas fill density) and kinetic simulations. Accurate modeling of the shock phase in ignition experiments essentially sets the initial conditions for hot-spot formation. The observed inaccuracies in standard hydrodynamic models for the surrogate implosions strongly suggest that the ignition experiments are not being accurately modeled.

ACKNOWLEDGMENTS

We thank the operations crews and engineering staff at NIF for supporting these experiments, and M. McKernan, M. Cairel, and M. Valadez for their work processing the CR-39.

This work is part of the first author's Ph.D. thesis, and was supported in part by the U.S. DoE (Grant No. DE-NA0001857, DE-FC52-08NA28752), LLNL (No. B597367), LLE (No. 415935- G), the Fusion Science Center at the University of Rochester (No. 524431), and the National Laser Users Facility (No. DE-NA0002035). This material is based upon work supported by the National Science Foundation Graduate Research Fellowship Program under Grant No. 1122374.

Appendix A: Sample Analysis

For the sample spectrum shown in Fig. 4, the results of the spectral analysis and subsequent ρR modeling are shown in Table I.

TABLE I: Results from the analysis of the D^3He proton spectrum for N101004-002-999 on DIM 90-78.

Quantity	Value	± random	± systematic[a]	± model
Energy (MeV)	11.34	0.10	0.10	
σ (MeV)	0.43	0.10	n/a	
Yield	8.71×10^7	0.94×10^7	n/a	
ρR (mg/cm^2)	96.0	3.1	6.1	5.3
R_{cm} (μm)	242	5	35	34

[a] Includes model uncertainty

Error bars are 1σ. For the proton energy, the system-

atic uncertainty primarily comes from the energy calibration of the WRFs[48], and random uncertainty comes from a combination of factors such as the hohlraum, variation in CR-39 properties, and statistical uncertainty. For the yield and line width, there are no systematic uncertainties, and the random uncertainties are primarily variation in CR-39 and statistics.

The energy uncertainties propagate to the modeled quantities ρR and R_{cm}. The systematic uncertainties for these quantities also include, and are dominated by, the modeling uncertainty. The model uncertainty is also listed separately in Table I.

Appendix B: Hohlraum Corrections

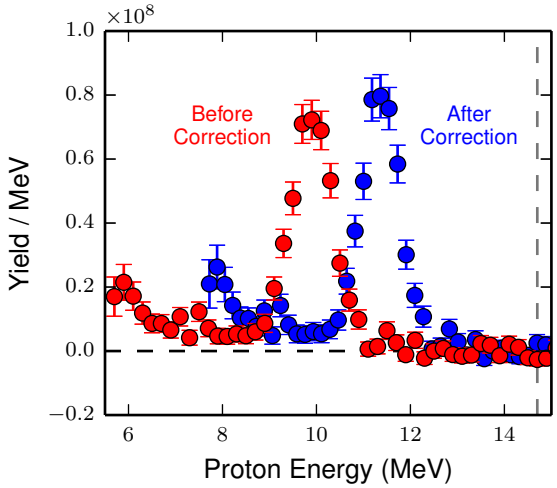

FIG. 21: Sample D^3He proton spectrum from NIF shot N101004-002-999, measured on the equator (DIM 90-78) before (red) and after (blue) hohlraum correction. In this case, the hohlraum thickness was 24.2 ± 1 μm of Au and 74.1 ± 3 μm of Al.

WRFs fielded on the equator always look through the hohlraum wall in indirect-drive experiments at the NIF. The large patches that would be required to give a clear line of sight for the 4 WRFs that are fielded on DIM 90-78 would unacceptably impact the implosion performance.

In addition to the high-Z hohlraum wall, which is made of Au or DU, there is a Thermo-Mechanical Package (TMP) made of thin aluminum. For most experiments, the hohlraum wall profile is defined by engineering drawings, and the energy correction due to the hohlraum wall is done by calculating the average thickness intercepted by the WRF line-of-sight. The uncertainties in hohlraum thickness (± 1 μm for the hohlraum wall, and ± 3 μm for the TMP) are standard tolerances, and these uncertainties are propagated through the analysis. In this case, the hohlraum uncertainty contributes ± 56 keV of uncertainty to the final determined energy.

The actual energy correction is applied to the entire spectrum, as shown in Fig. 21 by shifting each energy using cold-matter stopping powers[49]. The use of cold-matter stopping power in the hohlraum wall is a good approximation and has been checked against fully-integrated radiation-hydrodynamics hohlraum calculations. Because of the non-linearity in stopping power with proton energy, lower proton energies experience more downshift than higher energy protons, which has an 'accordion' effect on the spectrum, though a Gaussian shape is maintained for the energies in this work ($\gtrsim 5$ MeV).

For some hohlraum designs a 'bump' feature is present in the WRF line of sight. During the laser pulse a shock passes through the wall, and in the bump material flows laterally out of the line of sight. This situation is calculated with 2-D radiation-hydrodynamic simulations, and the wall thickness is corrected based on these simulations.

Appendix C: Implosion Model Parameterization

Typical parameters and assumptions in the 1-D implosion model are shown in Table II with uncertainties. The first six (shell material, inner and outer radius, fuel pressure, and fuel fill) are determined from a database of shot setup parameters. The values shown in the table are typical numbers. For the shell material, the ablator dopant (Ge or Si) is included, though the dopant level ($\sim 1\%$) has negligible effect on the inferred quantities. The following 10 parameters are treated as assumptions in the model and characterize the in-flight properties of the implosion. The ablated mass density profile (defined by $\rho_{\max}$, $\rho_{\min}$, and λ) is given in Eq. 7.

For the assumed in-flight conditions, experimental data is used in the choice of value whenever possible. The shell thickness and mass remaining are measured with x-ray radiography[8] and typical values from that data are used here. The temperature profile and ablated mass density profile are unmeasured, and thus typical values are taken from HYDRA calculations where the implosion trajectory (i.e. bang time) is well matched. Since the simulation may not accurately represent the experimental conditions, large uncertainties are assigned to these values (see Table II).

In the table we also give the resulting uncertainties in ρR for shot N101004 (see also Fig. 4 and Appendix A) resulting directly from the uncertainties in the model parameters. The dominant sources are the uncertainty in fuel temperature, ablated mass density profile (collectively from $\rho_{\max}$, $\rho_{\min}$, and λ), in-flight shell thickness, and mass remaining. The other sources of uncertainty are negligible ($\ll 1$ mg/cm^2). The shell thickness has a smaller effect than might be expected, the reason for this is that it only affects the inferred ρR through the stopping power Coulomb logarithm.

A mix model was added to this framework to evaluate the potential impact of mix on the proton dE/dx,

TABLE II: Typical values used in the model

Parameter	**Value**	±	N101004 ±ρR mg/cm^2
Initial Conditions			
Shell Material[a]	CH	n/a	n/a
Inner Radius (μm)	900	5	0.05
Outer Radius (μm)	1100	5	0.0
Fuel fill (mg/cm^3)	6.3	0.1	0.06
Fuel D Fraction	0.3	0.0	0
Fuel ^{3}He fraction	0.7	0.0	0
In-flight Assumptions			
Gas T (keV)	3	2	4.43
Mix T (keV)	0.5	0.2	0.23
Shell T (keV)	0.2	0.1	0.23
Ablated mass T (keV)	0.3	0.1	0.01
$\rho_{\max}$ (g/cc)	1.5	0.5	1.02
$\rho_{\min}$ (g/cc)	0.1	0.05	1.25
λ (μm)	70	30	1.25
Mix Fraction[b]	0.5%	0.5%	0.16
Shell Thickness[c] (μm)	40	10	1.65
Mass Remaining[d]	17.5%	5%	1.10

[a] Dopant type and level included; typically 1.084 g/cc, 57.2% H, 42.3% C, and 0.5% O atomic plus mid-Z dopant (Ge or Si).
[b] Percentage of the initial shell mass
[c] Full width of the in-flight shell
[d] For surrogate implosions, the quoted mass remaining includes the surrogate mass of CH

primarily in the fuel where the electron temperature can be high. The modeled mix is a uniform CH mix into the fuel specified by the amount of the initial shell mass which is mixed. Even assuming an implausibly large variation in mix ($0-1$% of the initial shell) causes only a 0.3 mg/cm^2 difference in inferred ρR; since 1% mix corresponds to a mix mass of 25μg, about $\sim 10\times$ higher than the worst observed[50], we conclude that mix in unimportant for shock proton spectroscopy.

The primary effect of the changing density and temperature in the three regions is variation in the stopping power, which is shown in Fig. 22. The higher temperature in the fuel leads to a much higher energy Bragg peak. At high energy, the stopping power in the shell is lower than in the fuel or the ablated mass due to the higher density in the shell (leading to a smaller $\log\Lambda$).

A stated choice in this work, which affects the reported ρR values, is the model used to calculate the charged-particle stopping power. In these dense plasma regimes, no experimental data exists to differentiate between models. In this work, the Li-Petrasso theory[21] has been used. However, this choice represents a potential quasi-systematic uncertainty in the inferred values. The magnitude of this effect is investigated by evaluating the implosion model at equivalent nominal conditions but with various choices of stopping model. In particular, we choose Zimmerman's parameterization of the Maynard-Deutsch model[51,52] and the Brown-Preston-Singleton (BPS) model[53].

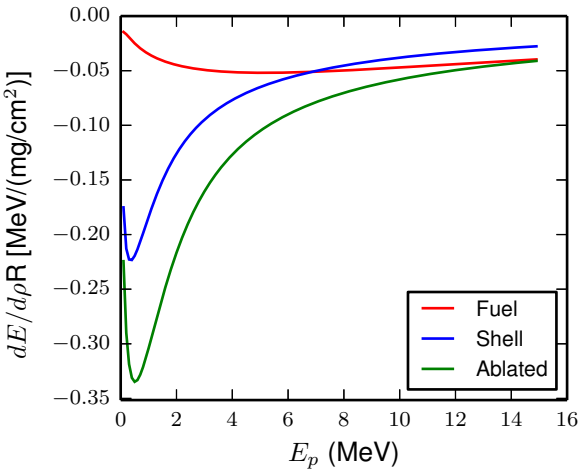

FIG. 22: Stopping power for the three components of the implosion model: fuel, shell, and ablated mass.

A comparison of the stopping power for the three models is shown in Fig. 23. The magnitude of the BPS and Zimmerman stopping are quite close. In the gas, these other two models have a smaller magnitude of dE/dx than Li-Petrasso, while they are higher in the shell and ablated material. A direct comparison of inferred ρR values using the implosion model and varying only the stopping model is shown in Fig. 24. For a wide range of relevant ρR, the Zimmerman and BPS stopping power would lead to an inferred ρR that is lower by ~ 10% or ~ 12% respectively.

Appendix D: Extension of the Implosion Model to 2- and 3-D

A simple extension of the implosion model to 2- and 3-D is essential for analysis of asymmetries observed between multiple detectors in these implosions, enabling the work presented in Ref. 19. An asymmetry is modeled as Legendre modes in the shape of the imploding shell:

$$R_{cm}(\theta,\phi) = \bar{R}\left[1+\Delta\times\sqrt{\frac{2\ell+1}{4\pi}\frac{(\ell-m)!}{(\ell+m)!}}e^{im\phi}P_\ell^m(\cos\theta)\right], \tag{D1}$$

where θ and ϕ are the polar and azimuthal angles, respectively, $\bar{R}$ is the unperturbed shell radius, Δ is the fractional asymmetry amplitude, and P_ℓ^m is an associated Legendre polynomial.

From the 1-D model presented in this paper, we have $\rho R(R_{cm})$. Areal density asymmetries in 2- or 3-D can

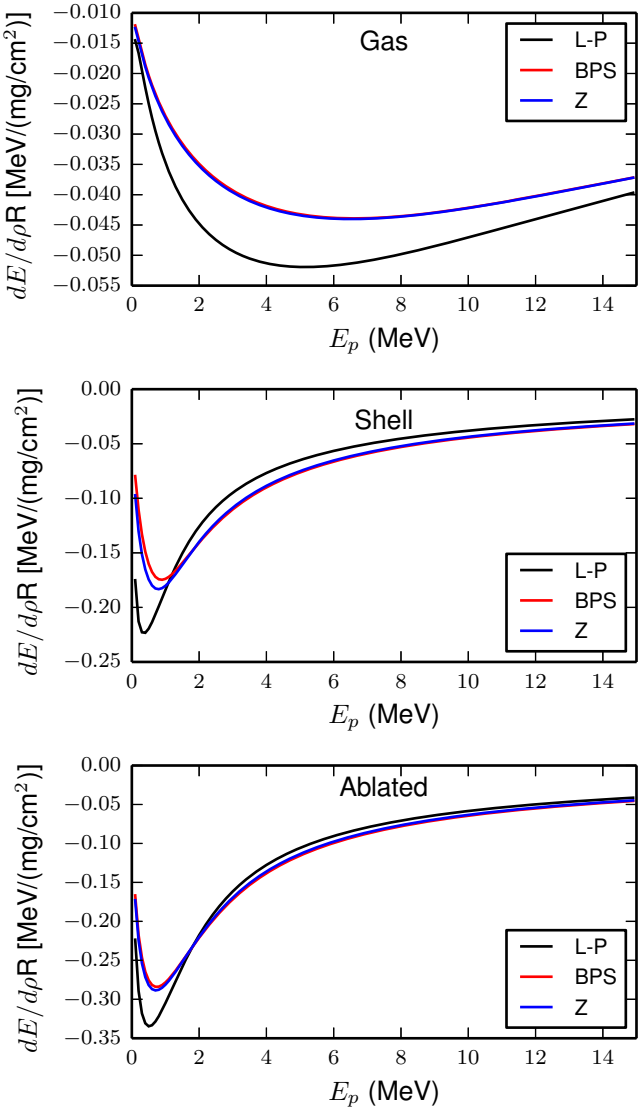

FIG. 23: Stopping power for the three models [Li-Petrasso (LP), Brown-Preston-Singleton (BPS), and Zimmerman (Z)] for each region of the implosion model: gas, shell, and ablated material.

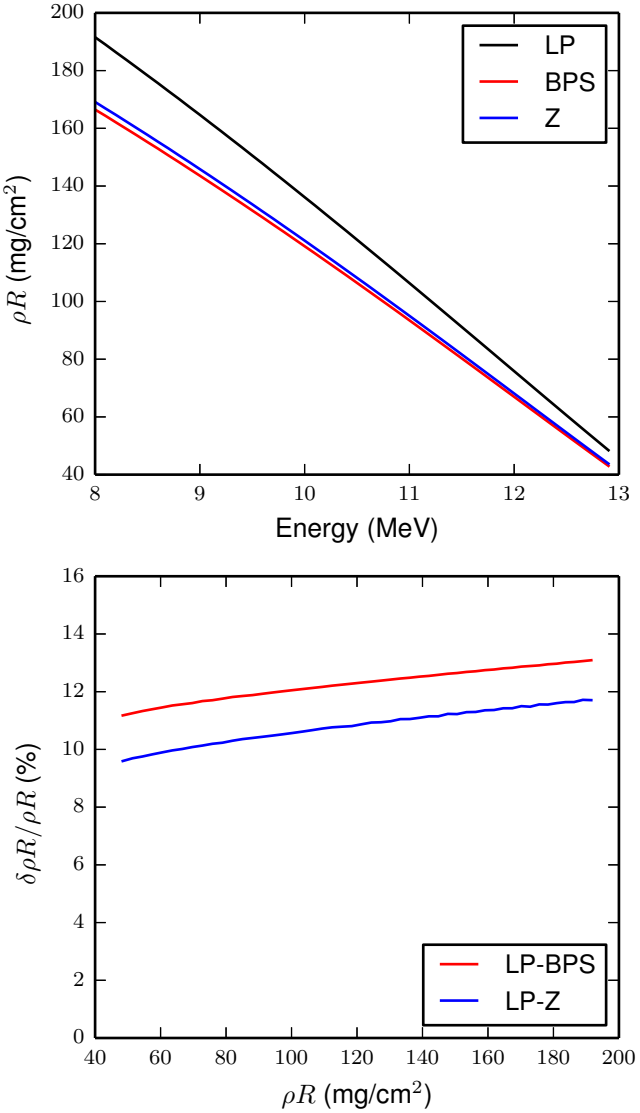

FIG. 24: Top: Inferred ρR versus final proton energy for three models [Li-Petrasso (LP), Brown-Preston-Singleton (BPS), and Zimmerman (Z)]. Bottom: Difference (%) between the Zimmerman or BPS models and Li-Petrasso.

thus be modeled as the convolution of $R_{cm}(\theta,\phi)$ and $\rho R(R_{cm})$ giving $\rho R(\theta,\phi,\bar{R},\Delta,\ell,m)$. The data points, each with their own coordinates (θ,ϕ), are then be fit using this convolution, where Δ and $\bar{R}$ are free parameters and ℓ, m are chosen.

An example of this analysis is shown in Fig. 25 for shot N101218-002-999. In this case a P_2 mode is assumed ($\ell = 2$, $m = 0$). The best fit parameters are $\bar{R} = 250 \pm 2\mu$m and $\Delta = -0.21 \pm 0.02$. The error bars are due to random/statistical errors only, excluding systematic detector calibration uncertainties and model uncertainties.

For the ConA2D implosions (see next section) in-flight 2-D x-ray radiography is used to measure the symmetry. Unfortunately the radiography requires large patches on the hohlraum wall, which induce a known $m = 2$ azimuthal asymmetry. This asymmetry is roughly aligned with the WRF equatorial line of sight, leading to an unconstrained problem between the modes $\ell = 2$ and $m = 2$ plus modes such as $\ell = 4$. To address this issue we use the radiography-measured mode amplitudes for the $\ell = 2$

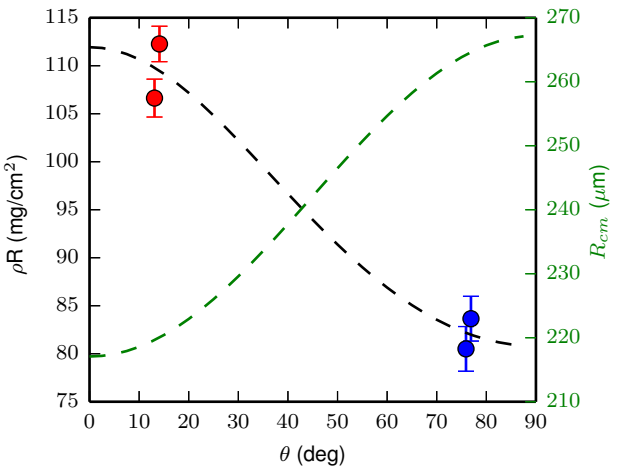

FIG. 25: ρR asymmetry analysis ($\ell = 2, m = 0$) for shot N101218-002-999, which had an usually large observed asymmetry. The polar (red) and equatorial (blue) data are shown with random/statistical errors only. The fit is shown as $\rho R(\theta)$ and $R_{cm}(\theta)$ (right axis).

and $\ell = 4$ and fit the amplitude of the $m = 2$ mode:

$$R_{cm}(\theta,\phi) = \bar{R}\left[1 + \Delta_{m=2}\sin\theta\cos(2\phi+\phi_0) + \Delta_{\ell=2}\times\sqrt{\frac{5}{4\pi}}P_2^0(\cos\theta) + \Delta_{\ell=4}\times\sqrt{\frac{9}{4\pi}}P_4^0(\cos\theta)\right], \quad \text{(D2)}$$

where $\Delta_{m=2}$ is the free parameter and ϕ_0 is taken as aligned with the equatorial line of sight (78°). The polar amplitudes $\Delta_{\ell=2}$ and $\Delta_{\ell=4}$ are determined from x-ray radiography.

Appendix E: Down-selected Data Summary

A summary of the data used in the shock dynamics analysis is shown in Table III.

[1] J. Nuckolls, L. Wood, A. Thiessen, and G. Zimmerman, Nature **239**, 139 (1972).
[2] J. Lindl, Physics of Plasmas **2**, 3933 (1995).
[3] G. Miller, E. Moses, and C. Wuest, Nuclear Fusion **44**, S228 (2004).
[4] O. L. Landen, T. R. Boehly, D. K. Bradley, D. G. Braun, D. A. Callahan, P. M. Celliers, G. W. Collins, E. L. Dewald, L. Divol, S. H. Glenzer, A. Hamza, D. G. Hicks, N. Hoffman, N. Izumi, O. S. Jones, R. K. Kirkwood, G. A. Kyrala, P. Michel, J. Milovich, D. H. Munro, A. Nikroo, R. E. Olson, H. F. Robey, B. K. Spears, C. A. Thomas, S. V. Weber, D. C. Wilson, M. M. Marinak, L. J. Suter, B. A. Hammel, D. D. Meyerhofer, J. Atherton, J. Edwards, S. W. Haan, J. D. Lindl, B. J. MacGowan, and E. I. Moses, Physics of Plasmas (1994-present) **17**, 056301 (2010).
[5] G. A. Kyrala, S. Dixit, S. Glenzer, D. Kalantar, D. Bradley, N. Izumi, N. Meezan, O. L. Landen, D. Callahan, S. V. Weber, J. P. Holder, S. Glenn, M. J. Edwards, P. Bell, J. Kimbrough, J. Koch, R. Prasad, L. Suter, J. L. Kline, and J. Kilkenny, Review of Scientific Instruments **81**, 10E316 (2010), http://dx.doi.org/10.1063/1.3481028.
[6] G. A. Kyrala, J. L. Kline, S. Dixit, S. Glenzer, D. Kalantar, D. Bradley, N. Izumi, N. Meezan, O. Landen, D. Callahan, S. V. Weber, J. P. Holder, S. Glenn, M. J. Edwards, J. Koch, L. J. Suter, S. W. Haan, R. P. J. Town, P. Michel, O. Jones, S. Langer, J. D. Moody, E. L. Dewald, T. Ma, J. Ralph, A. Hamza, E. Dzenitis, and J. Kilkenny, Physics of Plasmas (1994-present) **18**, 056307 (2011).
[7] D. Hicks, B. Spears, D. Braun, R. Olson, C. Sorce, P. Celliers, G. Collins, and O. Landen, Physics of Plasmas **17**, 102703 (2010).
[8] D. G. Hicks, N. B. Meezan, E. L. Dewald, A. J. Mackinnon, R. E. Olson, D. A. Callahan, T. Döppner, L. R. Benedetti, D. K. Bradley, P. M. Celliers, D. S. Clark, P. Di Nicola, S. N. Dixit, E. G. Dzenitis, J. E. Eggert, D. R. Farley, J. A. Frenje, S. M. Glenn, S. H. Glenzer, A. V. Hamza, R. F. Heeter, J. P. Holder, N. Izumi, D. H. Kalantar, S. F. Khan, J. L. Kline, J. J. Kroll, G. A. Kyrala, T. Ma, A. G. MacPhee, J. M. McNaney, J. D. Moody, M. J. Moran, B. R. Nathan, A. Nikroo, Y. P. Opachich, R. D. Petrasso, R. R. Prasad, J. E. Ralph, H. F. Robey, H. G. Rinderknecht, J. R. Rygg, J. D. Salmonson, M. B. Schneider, N. Simanovskaia, B. K. Spears, R. Tommasini, K. Widmann, A. B. Zylstra, G. W. Collins, O. L. Landen, J. D. Kilkenny, W. W. Hsing, B. J. MacGowan, L. J. Atherton, and M. J. Edwards, Physics of Plasmas (1994-present) **19**, 122702 (2012).
[9] G. Zimmerman and W. Kruer, Controlled Fusion **2**, 51 (1975).
[10] S. W. Haan, S. M. Pollaine, J. D. Lindl, L. J. Suter, R. L. Berger, L. V. Powers, W. E. Alley, P. A. Amendt, J. A. Futterman, W. K. Levedahl, M. D. Rosen, D. P. Rowley, R. A. Sacks, A. I. Shestakov, G. L. Strobel, M. Tabak, S. V. Weber, G. B. Zimmerman, W. J. Krauser, D. C. Wilson, S. V. Coggeshall, D. B. Harris, N. M. Hoffman, and B. H. Wilde, Physics of Plasmas (1994-present) **2**, 2480 (1995).
[11] M. Marinak, G. Kerbel, N. Gentile, O. Jones, D. Munro, S. Pollaine, T. Dittrich, and S. Haan, Physics of Plasmas **8**, 2275 (2001).
[12] D. G. Hicks, *Charged-Particle Spectroscopy: A New Window on Inertial Confinement Fusion* (Massachusetts Institute of Technology, 1999).
[13] R. D. Petrasso, J. A. Frenje, C. K. Li, F. H. Séguin, J. R. Rygg, B. E. Schwartz, S. Kurebayashi, P. B. Radha, C. Stoeckl, J. M. Soures, J. Delettrez, V. Y. Glebov, D. D. Meyerhofer, and T. C. Sangster, Phys. Rev. Lett. **90**, 095002 (2003).
[14] C. K. Li, F. H. Sguin, J. A. Frenje, R. D. Petrasso, R. Rygg, S. Kurebayashi, B. Schwartz, R. L. Keck, J. A. Delettrez, J. M. Soures, P. W. McKenty, V. N. Goncharov, J. P. Knauer, F. J. Marshall, D. D. Meyerhofer, P. B. Radha, S. P. Regan, T. C. Sangster, W. Seka, and C. Stoeckl, Physics of Plasmas (1994-present) **10**, 1919 (2003).
[15] J. A. Frenje, C. K. Li, F. H. Seguin, J. Deciantis, S. Kurebayashi, J. R. Rygg, R. D. Petrasso, J. Delettrez, V. Y. Glebov, C. Stoeckl, F. J. Marshall, D. D. Meyerhofer, T. C. Sangster, V. A. Smalyuk, and J. M. Soures, Physics of Plasmas **11**, 2798 (2004).
[16] J. R. Rygg, *Shock Convergence and Mix Dynamics in Inertial Confinement Fusion* (Massachusetts Institute of Technology, 2006).
[17] T. Boehly, D. Brown, R. Craxton, R. Keck, J. Knauer, J. Kelly, T. Kessler, S. Kumpan, S. Loucks, S. Letzring, F. Marshall, R. McCrory, S. Morse, W. Seka, J. Soures, and C. Verdon, Optics Communications **133**, 495 (1997).
[18] A. B. Zylstra, J. A. Frenje, F. H. Séguin, M. J. Rosenberg, H. G. Rinderknecht, M. G. Johnson, D. T. Casey, N. Sinenian, M. J.-E. Manuel, C. J. Waugh, H. W. Sio, C. K. Li, R. D. Petrasso, S. Friedrich, K. Knittel, R. Bionta, M. McKernan, D. Callahan, G. W. Collins, E. Dewald, T. Döppner, M. J. Edwards,

TABLE III: Data summary of shots used in the shock dynamics analysis

Shot	Type	Hohlraum	Laser Energy (MJ)	Effective Power (TW)	Absorption	Rise Time (ns)	Coast Time (ns)	Average ρR (mg/cm^2)	Equatorial Shock Yield	R_{cm} (μm)	Δ_{BT} (ns)
N110728-001-999	Symcap	Au	1.39±0.03	368±7	0.83±0.03	2	1.94±0.11	91±13	$(3.8 \pm 1.3) \times 10^7$	247±36	
N111007-002-999	ConvAblW	Au	1.29±0.02	350±7	0.84±0.03	2	2.46±0.04	80±6	$(7.1 \pm 1.1) \times 10^7$	269±40	
N111011-004-999	ConvAbl	Au	1.27±0.02	346±7	0.86±0.03	2	2.55±0.04	82±11	$(1.1 \pm 0.1) \times 10^8$	265±40	-0.75 ± 0.16
N111013-001-999	Symcap	Au	1.24±0.02	367±7	0.84±0.03	2	2.52±0.05	88±11	$(6.3 \pm 1.4) \times 10^7$	252±38	
N111014-001-999	Symcap	Au	1.26±0.02	368±7	0.84±0.03	2	2.44±0.05	87±6	$(1.4 \pm 0.1) \times 10^8$	255±40	
N111106-002-999	Symcap	Au	1.27±0.02	365±7	0.83±0.03	2	2.48±0.08	84±12	$(9.2 \pm 2.6) \times 10^7$	260±40	
N111109-002-999	Symcap	Au	1.26±0.03	370±7	0.86±0.03	2	2.43±0.08	86±12	$(8.1 \pm 2.1) \times 10^7$	256±39	
N111119-002-999	ConvAblW	Au	1.17±0.02	342±7	0.85±0.03	2	2.51±0.04	77±10	$(5.5 \pm 0.9) \times 10^7$	277±43	
N111120-002-999	Symcap	Au	1.50±0.03	375±7	0.84±0.03	2	1.74±0.08	94±12	$(1.6 \pm 0.2) \times 10^8$	242±36	
N111219-001-999	ConvAblW	Au	1.41±0.02	353±7	0.85±0.03	2	1.95±0.10	92±12	$(1.1 \pm 0.2) \times 10^8$	245±38	
N111220-002-999	ConvAblW	Au	1.41±0.03	352±7	0.84±0.03	1	2.03±0.10	89±12	$(1.6 \pm 0.3) \times 10^8$	251±38	
N120408-001-999	ConvAbl	U	1.52±0.03	292±5	0.81±0.03	3	0.92±0.05	139±10	$(3.0 \pm 0.4) \times 10^7$	191±28	-0.34 ± 0.12
N120409-001-999	ConvAbl	U	1.65±0.03	350±7	0.86±0.02	2	1.01±0.05	137±9	$(1.0 \pm 0.1) \times 10^8$	193±29	-0.38 ± 0.13
N120418-001-999	ConvAbl	U	1.70±0.03	336±6	0.82±0.03	3	1.12±0.05	152±10	$(2.1 \pm 0.4) \times 10^7$	181±29	-0.31 ± 0.13
N120421-006-999	ConvAbl	Au	1.63±0.03	306±6	0.85±0.03	3	1.04±0.06	133±9	$(3.4 \pm 0.1) \times 10^7$	196±28	-0.46 ± 0.13
N120629-002-999	ConvAblW	U	1.34±0.03	297±6	0.84±0.02	3	1.61±0.06	138±10	$(2.5 \pm 0.2) \times 10^7$	191±27	
N120709-003-999	ConvAblW	Au	1.57±0.03	298±6	0.85±0.03	3	1.15±0.06	137±9	$(1.8 \pm 0.2) \times 10^7$	192±28	
N120726-003-999	Symcap	Au	1.37±0.03	345±7	0.84±0.02	2	2.31±0.06	105±7	$(4.3 \pm 0.3) \times 10^7$	226±36	
N120909-001-999	Symcap	Au	1.43±0.03	370±7	0.86±0.02	2	2.00±0.05	81±13	$(1.4 \pm 0.6) \times 10^7$	266±42	
N120910-001-999	Symcap	Au	1.46±0.03	376±8	0.86±0.02	2	2.06±0.05	92±6	$(5.1 \pm 0.7) \times 10^7$	245±38	
N121008-002-999	ConvAblW	U	1.28±0.03	290±5	0.86±0.02	3	1.68±0.09	149±11	$(2.0 \pm 0.2) \times 10^7$	183±26	
N121202-001-999	ConvAbl2D	Au	1.28±0.03	315±7	0.86±0.02	2	1.97±0.09	110±8	$(2.4 \pm 0.2) \times 10^7$	219±31	-0.60 ± 0.13
N121210-001-999	ConvAbl2D	Au	1.28±0.03	315±7	0.86±0.02	2	1.99±0.09	110±7	$(2.4 \pm 0.2) \times 10^7$	219±31	-0.60 ± 0.13
N121218-004-999	ConvAbl2D	Au	1.29±0.03	317±7	0.87±0.02	2	2.02±0.09	107±7	$(2.2 \pm 0.2) \times 10^7$	223±32	-0.60 ± 0.13
N121219-001-999	ConvAbl2D	Au	1.29±0.03	302±7	0.87±0.02	2	2.01±0.09	119±8	$(3.5 \pm 0.3) \times 10^7$	209±31	-0.57 ± 0.13
N130211-003-999	ConvAbl2D	Au	1.28±0.03	325±6	0.91±0.03	2	2.04±0.09	110±8	$(5.5 \pm 0.3) \times 10^7$	220±32	-0.58 ± 0.13
N130212-001-999	ConvAbl2D	Au	1.27±0.03	321±6	0.90±0.03	2	2.18±0.09	100±7	$(6.2 \pm 0.5) \times 10^7$	233±33	-0.61 ± 0.13
N130213-002-999	ConvAbl2D	Au	0.96±0.02	222±4	0.91±0.03	2	2.66±0.09	105±8	$(8.7 \pm 0.8) \times 10^6$	226±32	-0.79 ± 0.19
N130226-002-999	ConvAbl2D	Au	1.28±0.02	323±5	0.90±0.03	2	1.95±0.09	100±7	$(5.0 \pm 0.5) \times 10^7$	233±34	-0.71 ± 0.13
N130227-002-999	ConvAbl2D	Au	1.28±0.02	322±4	0.89±0.03	2	2.13±0.09	98±7	$(6.4 \pm 0.6) \times 10^7$	236±33	-0.71 ± 0.12

S. Glenzer, D. G. Hicks, O. L. Landen, R. London, A. Mackinnon, N. Meezan, R. R. Prasad, J. Ralph, M. Richardson, J. R. Rygg, S. Sepke, S. Weber, R. Zacharias, E. Moses, J. Kilkenny, A. Nikroo, T. C. Sangster, V. Glebov, C. Stoeckl, R. Olson, R. J. Leeper, J. Kline, G. Kyrala, and D. Wilson, Review of Scientific Instruments **83**, 10D901 (2012).

[19]A. B. Zylstra *et al.*, submitted to Phys. Rev. E (2014).

[20]The proton velocity is high relative to the electron thermal velocity in these regimes, so electron stopping dominates.

[21]C. Li and R. Petrasso, Physical Review Letters **70**, 3059 (1993).

[22]G. Guderley, Luftfahrtforsch **19**, 302 (1942).

[23]P. M. Celliers, D. K. Bradley, G. W. Collins, D. G. Hicks, T. R. Boehly, and W. J. Armstrong, Review of Scientific Instruments **75**, 4916 (2004).

[24]H. F. Robey, P. M. Celliers, J. L. Kline, A. J. Mackinnon, T. R. Boehly, O. L. Landen, J. H. Eggert, D. Hicks, S. Le Pape, D. R. Farley, M. W. Bowers, K. G. Krauter, D. H. Munro, O. S. Jones, J. L. Milovich, D. Clark, B. K. Spears, R. P. J. Town, S. W. Haan, S. Dixit, M. B. Schneider, E. L. Dewald, K. Widmann, J. D. Moody, T. D. Döppner, H. B. Radousky, A. Nikroo, J. J. Kroll, A. V. Hamza, J. B. Horner, S. D. Bhandarkar, E. Dzenitis, E. Alger, E. Giraldez, C. Castro, K. Moreno, C. Haynam, K. N. LaFortune, C. Widmayer, M. Shaw, K. Jancaitis, T. Parham, D. M. Holunga, C. F. Walters, B. Haid, T. Malsbury, D. Trummer, K. R. Coffee, B. Burr, L. V. Berzins, C. Choate, S. J. Brereton, S. Azevedo, H. Chandrasekaran, S. Glenzer, J. A. Caggiano, J. P. Knauer, J. A. Frenje, D. T. Casey, M. Gatu Johnson, F. H. Séguin, B. K. Young, M. J. Edwards, B. M. Van Wonterghem, J. Kilkenny, B. J. MacGowan, J. Atherton, J. D. Lindl, D. D. Meyerhofer, and E. Moses, Phys. Rev. Lett. **108**, 215004 (2012).

[25]H. F. Robey, J. D. Moody, P. M. Celliers, J. S. Ross, J. Ralph, S. Le Pape, L. Berzak Hopkins, T. Parham, J. Sater, E. R. Mapoles, D. M. Holunga, C. F. Walters, B. J. Haid, B. J. Kozioziemski, R. J. Dylla-Spears, K. G. Krauter, G. Frieders, G. Ross, M. W. Bowers, D. J. Strozzi, B. E. Yoxall, A. V. Hamza, B. Dzenitis, S. D. Bhandarkar, B. Young, B. M. Van Wonterghem, L. J. Atherton, O. L. Landen, M. J. Edwards, and T. R. Boehly, Phys. Rev. Lett. **111**, 065003 (2013).

[26]J. D. Moody, D. A. Callahan, D. E. Hinkel, P. A. Amendt, K. L. Baker, D. Bradley, P. M. Celliers, E. L. Dewald, L. Divol, T. Döppner, D. C. Eder, M. J. Edwards, O. Jones, S. W. Haan, D. Ho, L. B. Hopkins, N. Izumi, D. Kalantar, R. L. Kauffman, J. D. Kilkenny, O. Landen, B. Lasinski, S. LePape, T. Ma, B. J. MacGowan, S. A. MacLaren, A. J. Mackinnon, D. Meeker, N. Meezan, P. Michel, J. L. Milovich, D. Munro, A. E. Pak, M. Rosen, J. Ralph, H. F. Robey, J. S. Ross, M. B. Schneider, D. Strozzi, E. Storm, C. Thomas, R. P. J. Town, K. L. Widmann, J. Kline, G. Kyrala, A. Nikroo, T. Boehly, A. S. Moore, and S. H. Glenzer, Physics of Plasmas **21**, 056317 (2014), http://dx.doi.org/10.1063/1.4876966.

[27]R. P. J. Town, D. K. Bradley, A. Kritcher, O. S. Jones, J. R. Rygg, R. Tommasini, M. Barrios, L. R. Benedetti, L. F. Berzak Hopkins, P. M. Celliers, T. Döppner, E. L. Dewald, D. C. Eder, J. E. Field, S. M. Glenn, N. Izumi, S. W. Haan, S. F. Khan, J. L. Kline, G. A. Kyrala, T. Ma, J. L. Milovich, J. D. Moody, S. R. Nagel, A. Pak, J. L. Peterson, H. F. Robey, J. S. Ross, R. H. H. Scott, B. K. Spears, M. J. Edwards, J. D. Kilkenny, and O. L. Landen, Physics of Plasmas (1994-present) **21**, 056313 (2014), http://dx.doi.org/10.1063/1.4876609.

[28]M. J. Rosenberg, H. G. Rinderknecht, N. M. Hoffman, P. A. Amendt, S. Atzeni, A. B. Zylstra, C. K. Li, F. H. Séguin, H. Sio, M. G. Johnson, J. A. Frenje, R. D. Petrasso, V. Y. Glebov, C. Stoeckl, W. Seka, F. J. Marshall, J. A. Delettrez, T. C. Sangster, R. Betti, V. N. Goncharov, D. D. Meyerhofer, S. Skupsky, C. Bellei, J. Pino, S. C. Wilks, G. Kagan, K. Molvig, and A. Nikroo, Phys. Rev. Lett. **112**, 185001 (2014).

[29]H. G. Rinderknecht, H. Sio, C. K. Li, A. B. Zylstra, M. J. Rosenberg, P. Amendt, J. Delettrez, C. Bellei, J. A. Frenje, M. Gatu Johnson, F. H. Séguin, R. D. Petrasso, R. Betti, V. Y. Glebov, D. D. Meyerhofer, T. C. Sangster, C. Stoeckl, O. Landen, V. A. Smalyuk, S. Wilks, A. Greenwood, and A. Nikroo, Phys. Rev. Lett. **112**, 135001 (2014).

[30]The thicknesses of the in-flight shell can change depending on the laser drive. In 'short-coast' implosions the laser drive is on for a longer time, whereas 'long-coast' implosions can have shell decompression due to time-truncated drive. However, the modeling reveals that this effect is not significant for interpreting this data, since the shell decompression does not significantly affect the ρR while the shell is at $R_{cm} \sim 250\mu$m.

[31]F. H. Séguin, J. A. Frenje, C. K. Li, D. G. Hicks, S. Kurebayashi, J. R. Rygg, B.-E. Schwartz, R. D. Petrasso, S. Roberts, J. M. Soures, D. D. Meyerhofer, T. C. Sangster, J. P. Knauer, C. Sorce, V. Y. Glebov, C. Stoeckl, T. W. Phillips, R. J. Leeper, K. Fletcher, and S. Padalino, Review of Scientific Instruments **74**, 975 (2003).

[32]F. H. Séguin, N. Sinenian, M. Rosenberg, A. Zylstra, M. J.-E. Manuel, H. Sio, C. Waugh, H. G. Rinderknecht, M. G. Johnson, J. Frenje, C. K. Li, R. Petrasso, T. C. Sangster, and S. Roberts, Review of Scientific Instruments **83**, 10D908 (2012).

[33]W. J. Hibbard, M. D. Landon, M. D. Vergino, F. D. Lee, and J. A. Chael, Review of Scientific Instruments **72**, 530 (2001).

[34]C. K. Li, F. H. Séguin, J. A. Frenje, R. D. Petrasso, P. A. Amendt, R. P. J. Town, O. L. Landen, J. R. Rygg, R. Betti, J. P. Knauer, D. D. Meyerhofer, J. M. Soures, C. A. Back, J. D. Kilkenny, and A. Nikroo, Phys. Rev. Lett. **102**, 205001 (2009).

[35]C. K. Li, F. H. Séguin, J. A. Frenje, M. Rosenberg, R. D. Petrasso, P. A. Amendt, J. A. Koch, O. L. Landen, H. S. Park, H. F. Robey, R. P. J. Town, A. Casner, F. Philippe, R. Betti, J. P. Knauer, D. D. Meyerhofer, C. A. Back, J. D. Kilkenny, and A. Nikroo, Science **327**, 1231 (2010), http://www.sciencemag.org/content/327/5970/1231.full.pdf.

[36]C. K. Li, A. B. Zylstra, J. A. Frenje, F. H. Séguin, N. Sinenian, R. D. Petrasso, P. A. Amendt, R. Bionta, S. Friedrich, G. W. Collins, E. Dewald, T. Döppner, S. H. Glenzer, D. G. Hicks, O. L. Landen, J. D. Kilkenny, A. J. Mackinnon, N. Meezan, J. Ralph, J. R. Rygg, J. Kline, and G. Kyrala, New Journal of Physics **15**, 025040 (2013).

[37]J. Lindl, O. Landen, J. Edwards, E. Moses, and N. Team, Physics of Plasmas **21**, 020501 (2014), http://dx.doi.org/10.1063/1.4865400.

[38]J. R. Rygg, O. S. Jones, J. E. Field, M. A. Barrios, L. R. Benedetti, G. W. Collins, D. C. Eder, M. J. Edwards, J. L. Kline, J. J. Kroll, O. L. Landen, T. Ma, A. Pak, J. L. Peterson, K. Raman, R. P. J. Town, and D. K. Bradley, Phys. Rev. Lett. **112**, 195001 (2014).

[39]R. Drake, *High-Energy-Density-Physics* (Springer, 2006).

[40]For simulations of NIF low-adiabat implosions to match the data, in particular the shock timing, implosion trajectory (r vs t), and bang time, multipliers must be applied throughout the pulse to decrease the effective drive on the implosion by a time-varying fraction[8,54].

[41]M. J. Edwards, P. K. Patel, J. D. Lindl, L. J. Atherton, S. H. Glenzer, S. W. Haan, J. D. Kilkenny, O. L. Landen, E. I. Moses, A. Nikroo, R. Petrasso, T. C. Sangster, P. T. Springer, S. Batha, R. Benedetti, L. Bernstein, R. Betti, D. L. Bleuel, T. R. Boehly, D. K. Bradley, J. A. Caggiano, D. A. Callahan, P. M. Celliers, C. J. Cerjan, K. C. Chen, D. S. Clark, G. W. Collins, E. L. Dewald, L. Divol, S. Dixit, T. Doeppner, D. H. Edgell, J. E. Fair, M. Farrell, R. J. Fortner, J. Frenje, M. G. Gatu Johnson, E. Giraldez, V. Y. Glebov, G. Grim, B. A. Hammel, A. V. Hamza, D. R. Harding, S. P. Hatchett, N. Hein, H. W. Herrmann, D. Hicks, D. E. Hinkel, M. Hoppe, W. W. Hsing, N. Izumi, B. Jacoby, O. S. Jones, D. Kalantar, R. Kauffman, J. L. Kline, J. P. Knauer, J. A. Koch, B. J. Kozioziemski, G. Kyrala, K. N. LaFortune, S. L. Pape, R. J. Leeper, R. Lerche, T. Ma, B. J. MacGowan, A. J. MacKinnon, A. Macphee, E. R. Mapoles, M. M. Marinak, M. Mauldin, P. W. McKenty, M. Meezan, P. A. Michel, J. Milovich, J. D. Moody, M. Moran, D. H. Munro, C. L. Olson, K. Opachich, A. E. Pak, T. Parham, H.-S. Park, J. E. Ralph, S. P. Regan, B. Remington, H. Rinderknecht, H. F. Robey, M. Rosen,

S. Ross, J. D. Salmonson, J. Sater, D. H. Schneider, F. H. Sguin, S. M. Sepke, D. A. Shaughnessy, V. A. Smalyuk, B. K. Spears, C. Stoeckl, W. Stoeffl, L. Suter, C. A. Thomas, R. Tommasini, R. P. Town, S. V. Weber, P. J. Wegner, K. Widman, M. Wilke, D. C. Wilson, C. B. Yeamans, and A. Zylstra, Physics of Plasmas (1994-present) **20**, 070501 (2013).

[42] J. R. Rygg, J. A. Frenje, C. K. Li, F. H. Séguin, R. D. Petrasso, D. D. Meyerhofer, and C. Stoeckl, Phys. Rev. E **80**, 026403 (2009).

[43] C. Cerjan, P. T. Springer, and S. M. Sepke, Physics of Plasmas **20**, 056319 (2013).

[44] Springer, P.T., Cerjan, C., Betti, R., Caggiano, J.A., Edwards, M.J., Frenje, J.A., Glebov, V.Yu., Glenzer, S.H., Glenn, S.M., Izumi, N., Jones, O., Kyrala, G., Ma, T., McNaney, J., Moran, M., Munro, D.H., Regan, S., Sangster, T.C., Sepke, S., Scott, H., Town, R.P.J., Weber, S.V., and Wilson, B., EPJ Web of Conferences **59**, 04001 (2013).

[45] H. Rinderknecht *et al.*, submitted to Phys. Rev. Lett. (2014).

[46] S. Le Pape, L. Divol, L. Berzak Hopkins, A. Mackinnon, N. B. Meezan, D. Casey, J. Frenje, H. Herrmann, J. McNaney, T. Ma, K. Widmann, A. Pak, G. Grimm, J. Knauer, R. Petrasso, A. Zylstra, H. Rinderknecht, M. Rosenberg, M. Gatu-Johnson, and J. D. Kilkenny, Phys. Rev. Lett. **112**, 225002 (2014).

[47] H. G. Rinderknecht, M. G. Johnson, A. B. Zylstra, N. Sinenian, M. J. Rosenberg, J. A. Frenje, C. J. Waugh, C. K. Li, F. H. Sguin, R. D. Petrasso, J. R. Rygg, J. R. Kimbrough, A. MacPhee, G. W. Collins, D. Hicks, A. Mackinnon, P. Bell, R. Bionta, T. Clancy, R. Zacharias, T. Döppner, H. S. Park, S. LePape, O. Landen, N. Meezan, E. I. Moses, V. U. Glebov, C. Stoeckl, T. C. Sangster, R. Olson, J. Kline, and J. Kilkenny, Review of Scientific Instruments **83**, 10D902 (2012).

[48] N. Sinenian, M. J.-E. Manuel, A. B. Zylstra, M. Rosenberg, C. J. Waugh, H. G. Rinderknecht, D. T. Casey, H. Sio, J. K. Ruszczynski, L. Zhou, M. G. Johnson, J. A. Frenje, F. H. Séguin, C. K. Li, R. D. Petrasso, C. L. Ruiz, and R. J. Leeper, Review of Scientific Instruments **83**, 043502 (2012).

[49] J. Ziegler, J. Biersack, and U. Littmark, *The stopping and range of ions in matter* (Pergamon, New York, 1985).

[50] T. Ma, P. K. Patel, N. Izumi, P. T. Springer, M. H. Key, L. J. Atherton, L. R. Benedetti, D. K. Bradley, D. A. Callahan, P. M. Celliers, C. J. Cerjan, D. S. Clark, E. L. Dewald, S. N. Dixit, T. Döppner, D. H. Edgell, R. Epstein, S. Glenn, G. Grim, S. W. Haan, B. A. Hammel, D. Hicks, W. W. Hsing, O. S. Jones, S. F. Khan, J. D. Kilkenny, J. L. Kline, G. A. Kyrala, O. L. Landen, S. Le Pape, B. J. MacGowan, A. J. Mackinnon, A. G. MacPhee, N. B. Meezan, J. D. Moody, A. Pak, T. Parham, H.-S. Park, J. E. Ralph, S. P. Regan, B. A. Remington, H. F. Robey, J. S. Ross, B. K. Spears, V. Smalyuk, L. J. Suter, R. Tommasini, R. P. Town, S. V. Weber, J. D. Lindl, M. J. Edwards, S. H. Glenzer, and E. I. Moses, Phys. Rev. Lett. **111**, 085004 (2013).

[51] G. Zimmerman, LLNL report, UCRL-JC-105616 (1990).

[52] G. Maynard and C. Deutsch, Phys. Rev. A **26**, 665 (1982).

[53] L. S. Brown, D. L. Preston, and R. L. S. Jr., Physics Reports **410**, 237 (2005).

[54] O. S. Jones, C. J. Cerjan, M. M. Marinak, J. L. Milovich, H. F. Robey, P. T. Springer, L. R. Benedetti, D. L. Bleuel, E. J. Bond, D. K. Bradley, D. A. Callahan, J. A. Caggiano, P. M. Celliers, D. S. Clark, S. M. Dixit, T. Doppner, R. J. Dylla-Spears, E. G. Dzentitis, D. R. Farley, S. M. Glenn, S. H. Glenzer, S. W. Haan, B. J. Haid, C. A. Haynam, D. G. Hicks, B. J. Kozioziemski, K. N. LaFortune, O. L. Landen, E. R. Mapoles, A. J. MacKinnon, J. M. McNaney, N. B. Meezan, P. A. Michel, J. D. Moody, M. J. Moran, D. H. Munro, M. V. Patel, T. G. Parham, J. D. Sater, S. M. Sepke, B. K. Spears, R. P. J. Town, S. V. Weber, K. Widmann, C. C. Widmayer, E. A. Williams, L. J. Atherton, M. J. Edwards, J. D. Lindl, B. J. MacGowan, L. J. Suter, R. E. Olson, H. W. Herrmann, J. L. Kline, G. A. Kyrala, D. C. Wilson, J. Frenje, T. R. Boehly, V. Glebov, J. P. Knauer, A. Nikroo, H. Wilkens, and J. D. Kilkenny, Physics of Plasmas (1994-present) **19**, 056315 (2012).